DOI: 10.3334/CDIAC/atg.ndp053

ORNL/CDIAC-85
NDP-053

Rattlesnake Mountain Observatory (46.4° N, 119.6° W) Multispectral Optical Depth Measurements: 1979–1994

N. R. Larson · J. J. Michalsky · B. A. LeBaron

R. C. Daniels, editor

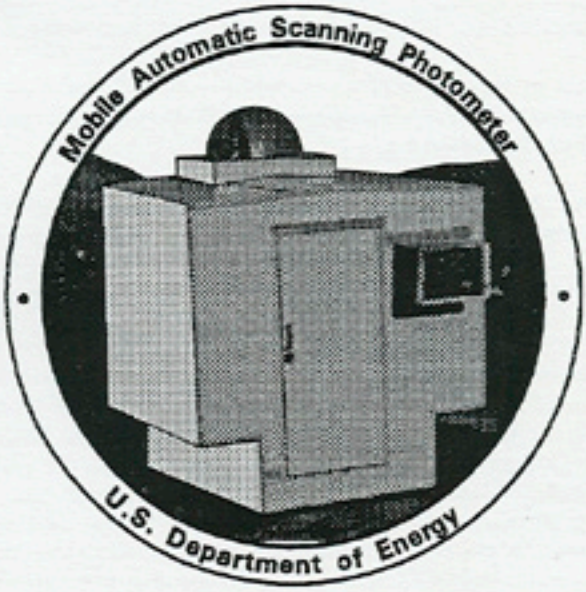

Carbon Dioxide Information Analysis Center
Oak Ridge National Laboratory

Environmental Sciences Division
Publication No. 4424

This report has been reproduced directly from the best available copy.

Available to DOE and DOE contractors from the Office of Scientific and Technical Information, P.O. Box 62, Oak Ridge, TN 37831; prices available from (615) 576-8401, FTS 626-8401.

Available to the public from the National Technical Information Service, U.S. Department of Commerce, 5285 Port Royal Rd., Springfield, VA 22161.

This report was prepared as an account of work sponsored by an agency of the United States Government. Neither the United States Government nor any agency thereof, nor any of their employees, makes any warranty, express or implied, or assumes any legal liability or responsibility for the accuracy, completeness, or usefulness of any information, apparatus, product, or process disclosed, or represents that its use would not infringe privately owned rights. Reference herein to any specific commercial product, process, or service by trade name, trademark, manufacturer, or otherwise, does not necessarily constitute or imply its endorsement, recommendation, or favoring by the United States Government or any agency thereof. The views and opinions of authors expressed herein do not necessarily state or reflect those of the United States Government or any agency thereof.

ORNL/CDIAC-85
NDP-053

RATTLESNAKE MOUNTAIN OBSERVATORY (46.4° N, 119.6° W) MULTISPECTRAL OPTICAL DEPTH MEASUREMENTS: 1979–1994

Contributed by

Nels R. Larson
Pacific Northwest Laboratory
Richland, Washington

Joseph J. Michalsky
Atmospheric Sciences Research Center
Albany, New York

Brock A. LeBaron
Utah Bureau of Air Quality
Salt Lake City, Utah

Edited by Richard C. Daniels[1]

Environmental Sciences Division
Publication No. 4424

Date Published: September 22, 1995

Prepared for the
Global Change Research Program
Environmental Sciences Division
Office of Health and Environmental Research
U.S. Department of Energy
Budget Activity Number KP 05 02 00 0

Prepared by the
Carbon Dioxide Information Analysis Center
OAK RIDGE NATIONAL LABORATORY
Oak Ridge, Tennessee 37831-6335
managed by
LOCKHEED MARTIN ENERGY SYSTEMS, INC.
for the
U.S. DEPARTMENT OF ENERGY
under contract DE-AC05-84OR21400

[1]Energy, Environment and Resources Center, The University of Tennessee, Knoxville, Tennessee.

TABLE OF CONTENTS

LIST OF FIGURES iv

LIST OF TABLES iv

ABSTRACT v

PART 1: INFORMATION ABOUT THE DATA PACKAGE 1
- 1. NAME OF THE NUMERIC DATA PACKAGE 3
- 2. CONTRIBUTORS 3
- 3. KEYWORDS 3
- 4. BACKGROUND INFORMATION 3
- 5. APPLICATIONS OF THE DATA 6
- 6. INSTRUMENTATION 6
- 7. DATA DERIVATION 8
- 8. KNOWN DATA LIMITATIONS 13
- 9. DATA CHECKS PERFORMED BY CDIAC 14
- 10. HOW TO OBTAIN THE DATA PACKAGE 15
- 11. REFERENCES 16

PART 2: INFORMATION ABOUT THE DIGITAL DATA FILES 17
- 12. CONTENTS OF THE MAGNETIC MEDIA 19
- 13. DESCRIPTIVE FILE ON THE MAGNETIC MEDIA 21
- 14. LISTING OF THE FORTRAN AND SAS™ DATA RETRIEVAL PROGRAMS 25
- 15. VERIFICATION OF DATA TRANSPORT 26

APPENDIX: PERTINENT LITERATURE 33

An assessment of the impact of volcanic eruptions on the Northern Hemisphere's aerosol burden during the last decade. By J.J. Michalsky, E.W. Pearson, and B.A. LeBaron. 1990.

A multipurpose computer-controlled scanning photometer. By E. W. Kleckner, J. J. Michalsky, L. L. Smith, J. R. Schmelzer, R. H. Severtsen, and J. L. Berndt. 1981.

LIST OF FIGURES

Figure 1. Locations and names of the eight stations that constituted the mobile automatic scanning photometer network. 4

Figure 2. Residual optical depths for the period August 1979 through September 1994, with volcanic and wildfire events identified. 5

Figure 3. Plot of the natural logarithm of the spectral irradiance at the surface [$\ln(I_\lambda)$] vs air-mass number (m). 10

Figure 4. Background aerosol levels for the Rattlesnake Mountain Observatory, Washington, at five wavelengths. 12

LIST OF TABLES

Table 1. List of the filters used by the computer-controlled scanning photometer for day and night operation. 7

Table 2. Rayleigh optical depths (τ_R) at the Rattlesnake Mountain Observatory. . . . 11

Table 3. List and description of the digital files. 19

Table 4. Variable formats for the eight flat ASCII data files. 24

Table 5. Statistical characteristics of the numeric variables in the eight ASCII data files. 26

ABSTRACT

Larson, N. R., Michalsky, J. J., and B. A. LeBaron. 1995. Rattlesnake Mountain Observatory (46.4° N, 119.6° W) Multispectral Optical Depth Measurements: 1979–1994. ORNL/CDIAC-85, NDP-053, Oak Ridge National Laboratory, Oak Ridge, Tennessee. 82 pp. doi: 10.3334/CDIAC/atg.ndp053

Surface measurements of solar irradiance of the atmosphere were made by a multipurpose computer-controlled scanning photometer at the Rattlesnake Mountain Observatory in eastern Washington. The observatory is located at 46.4° N, 119.6° W at an elevation of 1088 m above mean sea level. The photometer measures the attenuation of direct solar radiation for different wavelengths using 12 filters. Five of these filters (i.e., at 428 nm, 486 nm, 535 nm, 785 nm, and 1010 nm, with respective half-power widths of 2, 2, 3, 18, and 28 nm) are suitable for monitoring variations in the total optical depth of the atmosphere.

Total optical depths for the five wavelength bands were derived from solar irradiance measurements taken at the Rattlesnake Mountain Observatory from August 5, 1979, to September 2, 1994; these total optical depth data are distributed with this numeric data package (NDP). The total optical depth measurements are for the entire air column above the observation site. To determine the contribution of atmospheric aerosols to the total optical depths, the effects of Rayleigh scattering and ozone absorption were subtracted (other molecular scattering was minimal for the five filters) to obtain total column aerosol optical depths. The total aerosol optical depths were further decomposed into tropospheric and stratospheric components by calculating a robustly smoothed mean background optical depth (tropospheric component) for each wavelength using data obtained during periods of low stratospheric aerosol loading. By subtracting the smoothed background tropospheric aerosol optical depths from the total aerosol optical depths, residual aerosol optical depths were obtained. These residuals are good estimates of the stratospheric aerosol optical depth at each wavelength and may be used to monitor the long-term effects of volcanic eruptions on the atmosphere.

These data are available as an NDP from the Carbon Dioxide Information Analysis Center (CDIAC), and the NDP consists of this document and a set of computerized data files. The documentation contains information about the methods used for acquiring each variable, detailed descriptions of file contents and formats, and a discussion of the restrictions and limitations of the data. The computerized files consist of eight flat ASCII data files, one FORTRAN and one SAS™ retrieval file, and a descriptive file. The ASCII data files contain total optical depths for the 428 nm, 486 nm, 535 nm, 785 nm, and 1010 nm wavelength bands; total column aerosol optical depths for each wavelength; and smoothed background tropospheric aerosol optical depths. All files are available on floppy diskette or on the Internet via CDIAC's anonymous File Transfer Protocol (FTP) and World Wide Web (WWW) server.

PART 1: INFORMATION ABOUT THE DATA PACKAGE

1. NAME OF THE NUMERIC DATA PACKAGE

Rattlesnake Mountain Observatory (46.4° N, 119.6° W)
Multispectral Optical Depth Measurements:
1979–1994

2. CONTRIBUTORS

Nels R. Larson
Pacific Northwest Laboratory
P.O. Box 999
Richland, Washington 99352-0999

Joseph J. Michalsky
Atmospheric Sciences Research Center
100 Fuller Road
Albany, New York 12205

Brock A. LeBaron
Utah Bureau of Air Quality
1950 West North Temple
P.O. Box 16690
Salt Lake City, Utah 84116-0690

3. KEYWORDS

Aerosol; albedo; climate change; optical depth; photometer; stratosphere; troposphere; volcanic aerosols

4. BACKGROUND INFORMATION

To obtain measurements of the total optical depth of the atmosphere at different wavelengths, Pacific Northwest Laboratory (PNL) developed a multipurpose computer-controlled scanning photometer (Kleckner et al. 1981). The instrument is capable of making measurements of the attenuation of direct solar radiation at 12 different wavelengths. Five of these wavelengths (i.e., 428 nm, 486 nm, 535 nm, 785 nm, and 1010 nm, with respective half-power widths of 2, 2, 3, 18, and 28 nm) were found suitable for monitoring variations in the atmosphere's optical depth (Michalsky and Stokes 1983; Pearson et al. 1988; Michalsky et al. 1990).

This numeric data package (NDP) contains data for these five wavelength bands as measured at the Rattlesnake Mountain Observatory in eastern Washington. The photometer used was put into operation in March 1979 and has provided continous data since August 1979. This NDP contains the data collected from August 5, 1979, to September 2, 1994. This photometer replaced one that had previously been in operation at Rattlesnake Mountain from early 1978 to March 1979. The photometer is operated by PNL, Richland, Washington, and is located at 46.4° N, 119.6° W at an elevation of 1088 m above mean sea level.

The Rattlesnake Mountain Observatory is one of eight sites (Fig. 1) where photometers were fielded in 1979 by a coalition of three funding agencies [Office of Basic Energy Sciences, Geosciences Research Program, U.S. Department of Energy (DOE); Office of Conservation and Solar Energy, DOE; and the Atmospheric Sciences Program, National Science Foundation]. The mobile automatic scanning photometer (MASP) network, which operated through 1981, consisted of ten instruments. Three of the units were funded to provide observations during the International Magnetospheric Study, two were funded to collect site-specific solar measurements, and the remaining five were used to provide both day and night measurements of visible emission features associated with aurora and airglow. Because of programmatic changes, the full MASP network was discontinued at the end of 1981. However, the Rattlesnake Mountain station, along with four others, continued to operate with funding from the Office of Basic Energy Sciences, Geosciences Research Program, DOE. Data collected from the full MASP network has been archived at PNL.

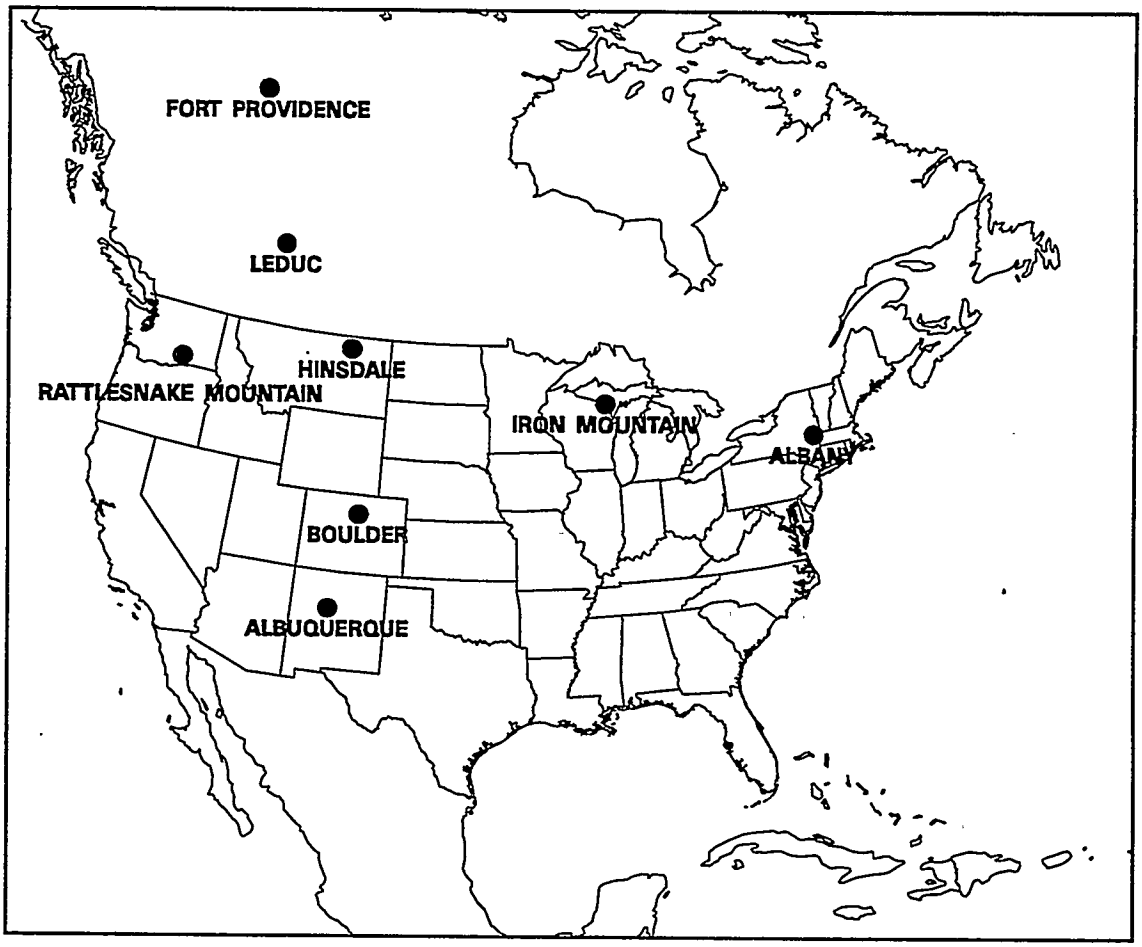

Figure 1. **Locations and names of the eight stations that constituted the mobile automatic scanning photometer network.**

The solar irradiance measurements taken at Rattlesnake Mountain may be used to monitor variations in the atmosphere's optical depth. In an undisturbed state, aerosols and dust particles tend to be concentrated into two layers in the atmosphere. The first, or troposphere, reaches from the Earth's surface to 12 to 15 km. Aerosols and dust in this layer are continuously affected by climate variations. Dust acts as nuclei around which water vapor condenses to produce cloud particles. Thus, the amount of dust and water vapor (determined by air temperature and vapor pressure) in the troposphere plays a major role in determining the atmosphere's total optical depth. In contrast the second layer, the stratosphere, is almost completely free of water vapor and dust when in an undisturbed state (Strahler and Strahler 1984).

An undisturbed stratosphere, at an altitude of 15 to 50 km, is relatively clean. Because of this, the stratosphere contributes several orders of magnitude less to the total optical depth of the atmosphere than does the troposphere. Large volcanic eruptions may inject materials to an altitude over 20 km, however. When this occurs, the stratosphere's optical depth may be enhanced such that its total optical thickness approaches that of the troposphere for up to 5 years, with 3 years being the norm (Jakosky 1986). This variation in stratospheric optical depth is shown in Fig. 2 for the period August 1979 through September 1994.

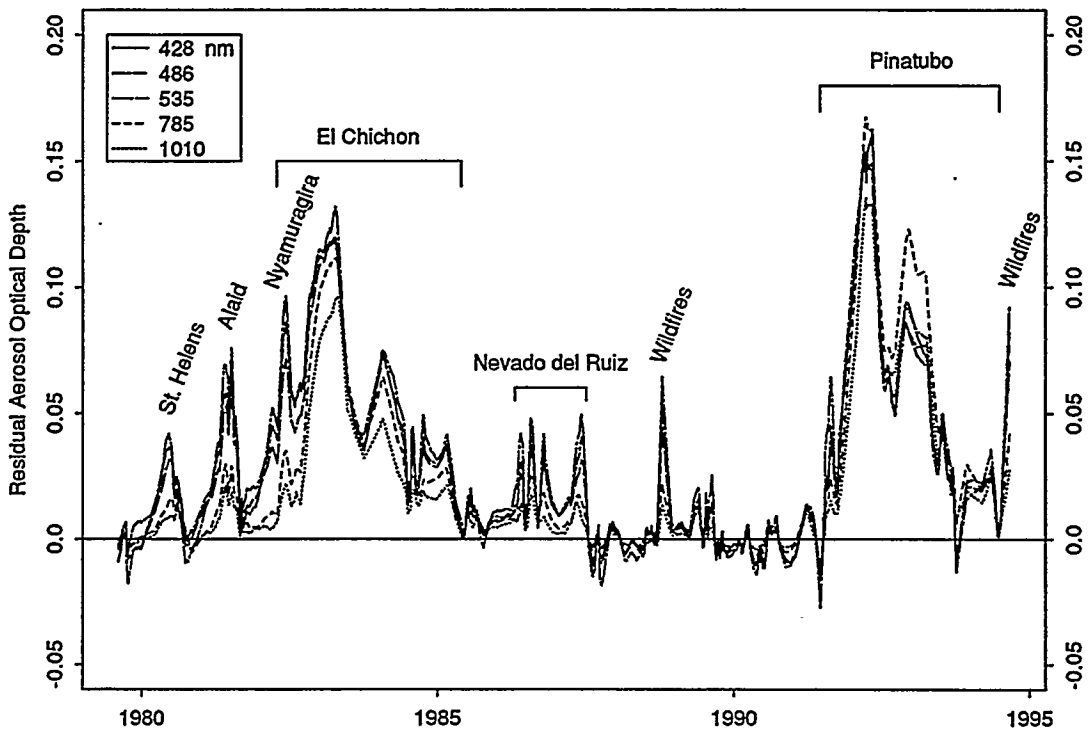

Figure 2. **Residual optical depths for the period August 1979 through September 1994, with volcanic and wildfire events identified.**

The presence of these dusts and aerosols acts to reduce the amount of solar energy that reaches the Earth's surface by scattering, absorbing, and reflecting incoming solar radiation. The concentration and size distribution of the attenuating aerosols in the atmosphere can be inferred based on optical depth and backscatter measurements taken using photometers, lidar, weather balloons, and satellites. Using these instruments it has been found that, in an undisturbed atmosphere, that aerosol size and optical depth varies seasonally in a predictable manner (Michalsky et al. 1990). This predictable monthly variation in particle size and optical depth, modulated by the redistribution of low- and high-pressure systems and aerosol source mechanisms from season to season, may be seen as the "natural" state of the atmosphere. The background optical depth (tropospheric optical depth) has been estimated and subtracted from instrument measurements to determine the impact of external perturbations on the stratosphere.

The injection of dust and aerosols from large volcanic eruptions can cause identifiable changes in the atmosphere's optical depth (Michalsky et al. 1984a, 1984b). The volcanic dust, mostly silicate particulate matter, falls out of the atmosphere within a few months, while the volcanic gases gradually oxidize and form sulfuric acid and other sulfates. These sulfates condense into liquid droplets that affect the solar absorption and scattering properties of the stratosphere (Hofman 1987). These aerosols intercept long-wave radiation radiating from the Earth's surface, thus changing its albedo and altering the heating and cooling processes that drive large-scale, high-altitude weather patterns.

5. APPLICATIONS OF THE DATA

The daytime solar data contained within this NDP may be useful to people involved in photovoltaic and photobiological research programs, to radiative transfer theorists, and to climate modelers interested in the attenuation of solar radiation by atmospheric aerosols, water vapor, and dust. The ability of these measurements to quantify, identify, and track the ageing process of volcanic aerosols is of interest in climate forecasting because the presence of unusually high concentrations of aerosols in the stratosphere may change the Earth's albedo, heat the stratosphere, cool or heat the surface (depending on the latitude of the eruption), and affect the strength and longevity of El Niño events (Jakosky 1986).

6. INSTRUMENTATION

The multipurpose computer-controlled scanning photometer used at Rattlesnake Mountain was initially developed to eliminate the tedium of tending a photometer during repeated sequences of all-sky scans. The scanning photometer uses a set of moving mirrors that transfers the incoming sun light or moon light into parallel rays that are measured by a stationary photometer. The photometer is currently equipped for day and night operation and is, in essence, a computer-controlled altazimuth telescope with 13-cm optics (Kleckner et al. 1981, see appendix). The day/night operation of the photometer is determined by a photometric threshold detector mounted on the outside of the instrument housing. Based on the status of this optical switch a day or night scanning mode is utilized. The photometer scans the sky using 5 filters during nighttime operation and 12 filters during the day (Table 1). The data contained within this NDP were obtained during daytime operation using the 428-, 486-, 535-, 785-, and 1010-nm filters.

Table 1. **List of the filters used by the computer-controlled scanning photometer for day and night operation.**

Filter wavelength (nm)	Half-power bandwidth (nm)	Period of operation	Filter characteristics
630	1	Night, Day	Contamination from O_2
558	1	Night, Day	Probable red leak
486	2	Night, Day	
428	2	Night, Day	
535	3	Night, Day	
395	60	Day	Wide pass band
470	100	Day	Wide pass band
570	100	Day	Wide pass band
680	120	Day	Contamination from O_2, H_2O
785	18	Day	
900	150	Day	Contamination from H_2O
1010	28	Day	

Note: Only data obtained using the highlighted filters are included in this database.

One of the problems with historic solar radiation measurements is the difficulty in determining the stability and error ratio of the instruments used in collecting the data. Detector stability for this photometer was insured by using a silicon photodiode that has a linear response to incident light of better than 1% and has a response to a standard light source of ±0.5% or better over 6 months. To counter the temperature dependence of photodiode response, the diode has been hermetically sealed in a package with the high-gain field-effect transistor (FET) input amplifier and is operated in a climate-controlled (20° ± 3° C) enclosure. This configuration provides an overall photodiode stability of better than 1% for all but the longest wavelength filter. This stability was confirmed during the side-by-side operation of two photometers in 1987 (Pearson et al. 1988).

The measurement routine used to obtain the direct-sun, daytime data samples begins at sunrise and is repeated every 5 minutes until sunset. In each 5-minute sampling interval, all 12 filter measurements are made one at a time by scanning across the Sun aureole and recording the peak scan intensities. This scanning process takes 2 minutes per sampling interval; during the remaining 3 minutes other measurements were not attempted with the instrument that produced this data set. The Sun's position is calculated once per minute to an accuracy of 0.5°. With the pointing accuracy of the instrument being 0.3°, the maximum error in pointing directly at the Sun is < 1°. To make the direct measurement a sun-centered raster scan is made. Each scan has dimensions of 5.0° in azimuth by 3.0° elevation and generates 110 samples. The largest raster value is then saved.

This sampling process results in the collection of 12 samples per hour for each of the 486-, 428-, 535-, 785-, and 1010-nm filters. To determine the total atmospheric optical depth

for each wavelength, the samples taken between air-mass numbers 2 and 6 during cloud-free intervals in the morning and afternoon are grouped into morning and afternoon observation sets (an air-mass number is the relative path length of solar radiation through the atmosphere to the photometer). Thus, the number of sets may vary from 0 to 2 per day, with the number of sample points used in each set varying based on daily changes in the Sun's declination during the year and the presence or absence of clouds.

This NDP includes observation sets taken during intervals when the atmosphere was stable. The data that the researchers used to infer each observation set was time-stamped based on the midpoint of the sampling points used. Because some sample points may have been deleted from each 2-to-6 air-mass interval due to clouds, the time stamp associated with each set does not simply define the midpoint for the 2-to-6 air-mass interval, but rather the mid-time between the first point and last point used in calculating the optical depth. For instance, the mid-sample time of each individual 5-minute scanning period is the start time of the scan plus 1 minute. The midpoint of these is reported as the time for the observation set (e.g., if five samples were used and their sample times were 8:01, 8:06, 8:11, 8:16, 8:31, 8:36, and 8:41, the time stamp for the observation set would be 8:21).

7. DATA DERIVATION

The solar radiation measurements taken by the computer-controlled photometer between air-mass numbers 2 and 6 are used to obtain a maximum of two observation sets per day (one in the morning and one in the afternoon). The radiation measurements obtained for each observation set are converted to total optical depths based on Eq. 1:

$$I_\lambda = I_{0\lambda} \bullet e^{-\tau m} , \qquad (1)$$

where I_λ is the spectral irradiance measured at the surface for wavelength λ, $I_{0\lambda}$ is the spectral irradiance for λ at the top of the atmosphere, τ is the total optical depth at λ in the zenith direction, and m is the equivalent air-mass in the direction of the Sun normalized to the mass of air in the zenith direction (i.e., relative atmospheric path length).

The spectral irradiance at the surface is measured directly by the photometer, irradiance at the top of the atmosphere is derived based on Langley regression, and m is the air-mass number of the samples used in the observation set. The m value for each sample is derived from Rozenberg's formula relating solar zenith angle to the air-mass number (Rozenberg 1966):

$$m = 1 \div [\cos(z) + 0.025 \bullet e^{-11.0 \bullet \cos(z)}] , \qquad (2)$$

where z is the solar zenith angle corrected for atmospheric refraction (if solar zenith angle = 0°, m ≈ 1). In this database, only samples taken between 2 and 6 air-masses have been used; this converts to time periods when the Sun is ~30° to 9.3° above the horizon.

Equation 1 can be rewritten, linearized (by taking the logarithm of I), and solved to determine the total optical depth. This leads to

$$\tau = \frac{\ln(I_{0\lambda}) - \ln(I_\lambda)}{m} . \tag{3}$$

To determine the value of $\ln(I_{0\lambda})$ and τ, a plot of $\ln(I_\lambda)$ vs m is made from the data samples in each observation set, and a linear least-squares regression is performed. The intercept and slope of the regression line are $\ln(I_{0\lambda})$ and τ, respectively. The process used in the analysis involves the following steps:

(1) Plot direct-normal irradiance for the 535-nm filter between 2 and 6 air-masses in the morning, and delete cloudy sample points from the observation set.

(2) Plot $\ln(I_\lambda)$ vs air-mass number (on the X-axis) for all wavelengths.

(3) Delete any sample point that is not a linear fit at all wavelengths.

(4) Replot and verify linearity of fit. A minimum span of 2 air-mass numbers between the first and last sample point is required.

(5) Save the final Langley regression. The intercept and slope of the regression line are $\ln(I_{0\lambda})$ and τ, respectively.

(6) Repeat steps 1 through 5 for the afternoon if clear-interval, direct-normal points exist.

Only observation sets that cover a minimum span of 2 air-masses between the first and the last sample point are included in the database. An example of one of these plots is shown in Fig. 3.

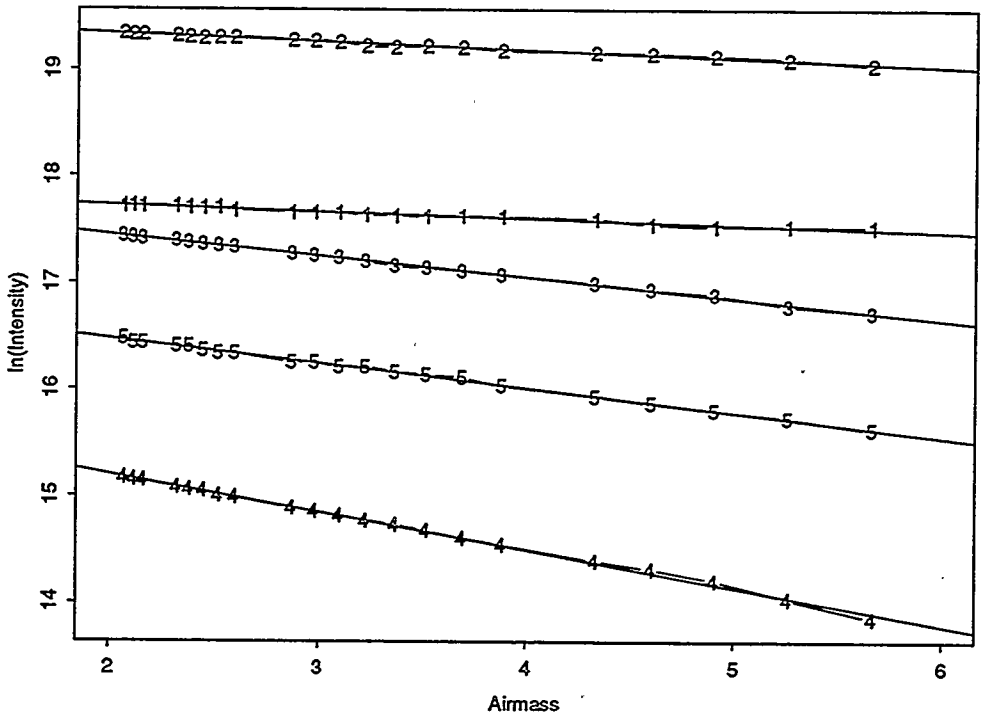

Figure 3. **Plot of the natural logarithm of the spectral irradiance at the surface [ln(I_λ)] vs air-mass number (m).**

The total optical depth at λ comprises four components and may be written as follows:

$$\tau = \tau_a + \tau_o + \tau_m + \tau_R \,, \tag{4}$$

where the subscripts denote aerosol, ozone, molecular, and Rayleigh optical depths. Values for τ_o, τ_m, and τ_R are known and can be subtracted from τ, leaving us with τ_a for each wavelength. Values for τ_o were estimated based on the work of Van Heuklon (1979), τ_R values have been calculated based on Eq. 5 (Hasen and Travis 1974) and the contribution of τ_m is assumed to be zero since the five filters were selected to avoid virtually all forms of gaseous molecular absorption.

$$\tau_R = \frac{0.008569}{\lambda^4} \bullet \left(1 + \frac{0.0113}{\lambda^2} + \frac{0.00013}{\lambda^4}\right) \bullet 0.878 \tag{5}$$

where λ is the wavelength in micrometers and 0.878 is the U.S. standard pressure in

atmospheres for an elevation of 1088 m. The calculated Rayleigh optical depths for Rattlesnake Mountain are shown in Table 2.

Table 2. Rayleigh optical depths (τ_R) at the Rattlesnake Mountain Observatory.

Band (nm)	Optical depth
1010	0.007311
785	0.020183
535	0.095607
486	0.141625
428	0.238906

The total aerosol optical depth measurements are for the total air column above the observation site and have an estimated error on the order of 0.01, which implies that many of the smaller values in the database are statistically insignificant. The effects of ozone, molecular, and Rayleigh scattering were subtracted to determine τ_a. When determining the contribution of the troposphere and stratosphere to τ_a it is necessary to partition τ_a into tropospheric and stratospheric components:

$$\tau_a = \tau_{trop} + \tau_{strat} \, . \tag{6}$$

The procedure for separating the total aerosol optical depth into its tropospheric and stratospheric components is based on the assumption that the aerosol optical depth of the troposphere, though highly variable, has a predictable underlying seasonal behavior (Michalsky et al. 1990, reprinted in Appendix A). Since local conditions may vary significantly from day to day, it is only possible to calculate and remove seasonal behavior by computing a robustly smoothed background column aerosol depth for each wavelength based on observation sets taken during periods of minimum stratospheric loading (Michalsky et al. 1988; Pearson et al. 1988). The background aerosol data were derived from measurements taken during periods of low stratospheric loading from June 15, 1987, to June 15, 1991, inclusive, folded into a single year. The "year" was then smoothed using the locally weighted regression method developed by Cleveland (1979). The background aerosol levels derived for Rattlesnake Mountain are shown in Fig. 4. By removing this seasonal behavior (τ_{trop}) from τ_a, the researchers derived a residual aerosol optical depth for each wavelength and assumed it to be the contribution from the stratosphere (τ_{strat}).

Thus, the equations described above were used to convert solar irradiance measurements taken at the surface to total optical depths for each wavelength. These total optical depths were then corrected for ozone and Rayleigh scattering (molecular scattering is minimal due to filter selection) and total column aerosol optical depths were obtained.

Estimates of τ_{trop} were then made and subtracted from τ_a to obtain the residual or estimated stratospheric aerosol optical depth for each wavelength.

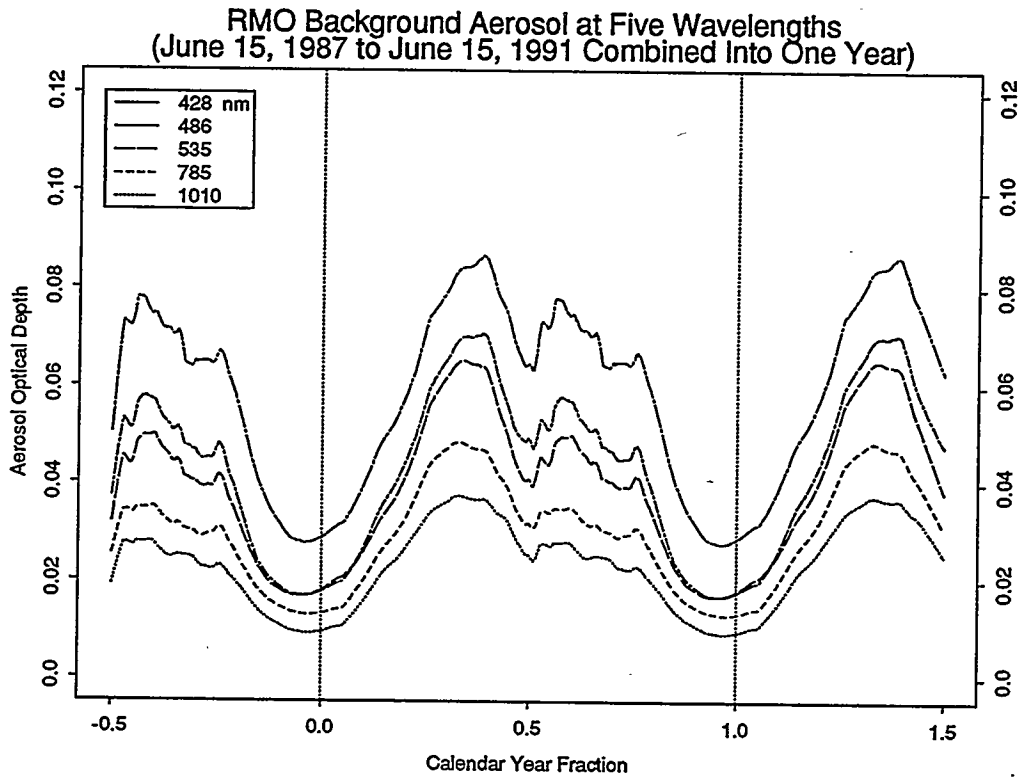

Figure 4. **Background aerosol levels for the Rattlesnake Mountain Observatory, Washington, at five wavelengths.**

8. KNOWN DATA LIMITATIONS

The following list shows the caveats that should be considered when these data are used. Failure to consider these limitations may result in erroneous interpretation of the data.

(1) Because of occasional cloudy weather, optical depth samples are taken irregularly, with a relative high frequency during the summer and lower frequency during the winter.

(2) The total optical depths were derived from samples taken between 2 and 6 air-masses in the morning and afternoon. Since the period of time between 2 and 6 air-masses changes throughout the year, the number of sample points used to calculate the optical depth for each observational set varies with a maximum in winter.

(3) The standard error of the Langley determination of total optical depth for each wavelength and observation set are included with this database. The maximum standard error is 0.0158, 0.0148, 0.025, 0.0235, 0.0282 for the 1010-nm, 785-nm, 535-nm, 486-nm, and 428-nm wavelengths, respectively.

(4) The procedure used to convert the total optical depths to aerosol optical depths has an estimated error of 0.01, which implies that some of the smaller aerosol values in this database are statistically insignificant.

(5) The background aerosol data were derived from measurements taken during periods of low stratospheric loading from June 15, 1987, to June 15, 1991, inclusive, folded into a single year. The "year" was then smoothed using the locally weighted regression method developed by Cleveland (1979).

9. DATA CHECKS PERFORMED BY CDIAC

An important part of the data packaging process at CDIAC is the quality assurance (QA) of the data before its distribution. Data received at CDIAC are rarely in perfect condition for immediate distribution, regardless of the source. Reviews conducted involved the examination of the data for completeness, reasonableness, and accuracy. The QA process is an important component in the value-added concept of assuring accurate, usable information for researchers. The following summarizes the QA checks performed on the various data groups presented in this document.

(1) The minimum, maximum, mean values and standard deviation were calculated for each numeric variable in each data file to check for outliers.

(2) The data for each wavelength were graphed and compared to a listing of known volcanic and wildfire events to ensure that large deviations from background aerosol optical depths occurred only following known atmospheric perturbations.

(3) The year.fraction time stamp for each observational set was intercompared with the unsmoothed total optical depth and aerosol files to ensure that they matched.

(4) The year.fraction was converted to a year:day:hour:minute format to check the reported beginning and ending dates of record.

10. HOW TO OBTAIN THE DATA PACKAGE

This publication describes the contents of the multispectral radiometric observations that are distributed with this documentation. These files are available on 8-mm tape, 0.25-in. tape cartridge, IBM-formatted floppy diskettes (high density, 3.5- or 5.25-inch diskettes), and through the Internet via anonymous File Transfer Protocol FTP (at cdiac.esd.ornl.gov) or the World Wide Web (at http://cdiac.esd.ornl.gov/cdiac/). Requests for the magnetic tape should include any specific instructions for transmitting the data as required by the user or the user's local computer system. Requests not accompanied by specific instructions will be filled on 3.5-in. high density diskette and formatted as given in Part 2, Section 12. Requests for this data package should be addressed to:

Carbon Dioxide Information Analysis Center
Oak Ridge National Laboratory
Post Office Box 2008
Oak Ridge, Tennessee 37831-6335
U.S.A.

Telephone: (423) 574-0390 or 574-3645
FAX: (423) 574-2232

BITNET: CDP@ORNLSTC
INTERNET: CDIAC@ORNL.GOV

The data files may be acquired via FTP from CDIAC's anonymous FTP service as follows:

- FTP to CDIAC.ESD.ORNL.GOV (128.219.24.36).
- Enter "anonymous" as the user identification.
- Enter your electronic mail address as the password (e.g., BUBBA@ORNL.GOV).
- Change to the data directory "cd pub/ndp053".
- Set FTP to get ASCII files by using the FTP "ascii" command.
- Acquire the input/output programs and data files using the FTP "mget *" command.

Contact CDIAC by phone, FAX, or electronic mail to order a hard copy of this documentation.

11. REFERENCES

Cleveland, W. S. 1979. Robust locally weighted regression and smoothing scatterplots. *Journal of the American Statistical Association* 74:829-836.

Hansen, J. E. and L. D. Travis. 1974. Light scattering in planetary atmospheres. *Space Science Reviews* 16:527-610.

Hofman, D. J. 1987. Perturbations to the global atmosphere associated with the El Chichon volcanic eruption of 1982. *Reviews of Geophysics* 25:743-759.

Jakosky, B. M. 1986. Volcanoes, the stratosphere, and climate. *Journal of Volcanology and Geothermal Research* 28:247-255.

Kleckner, E. W., Michalsky, J. J., Smith, L. L., Schmelzer, J. R., Severtson, R. H., and J. L. Berndt. 1981. *A Multipurpose Computer-Controlled Scanning Photometer*. PNL-4081, UC-37, Pacific Northwest Laboratory, Richland, Washington.

Michalsky, J. J. and G. M. Stokes. 1983. Mt. St. Helens' aerosols: some tropospheric and stratospheric effects. *Journal of Climate and Applied Meteorology* 22:640-648.

Michalsky, J. J., Herman, B. M., and N. R. Larson. 1984a. Mid-latitude stratospheric aerosol layer enhancement by El Chichon: the first year. *Geophysical Research Letters* 11:76-79.

Michalsky, J. J., Larson, N. R., and N. S. Laulainen. 1984b. Evolution of stratospheric aerosol size distribution from ground-based radiometric measurements: a study of El Chichon aerosol, pp 119-122. In *IRS'84: Current Problems in Atmospheric Radiation.* A. Deepak Publishing, Hampton, Virginia.

Michalsky, J. J., Pearson, E. W., and B. A. LeBaron. 1988. The ten-year pattern (1978-1987) of stratospheric aerosol loading using ground-based radiometry, pp 568-571. In *IRS'88: Current Problems in Atmospheric Radiation,* A. Deepak Publishing, Hampton, Virginia.

Michalsky, J. J., Pearson, E. W., and B. A. LeBaron. 1990. An assessment of the impact of volcanic eruptions on the Northern Hemisphere's aerosol burden during the last decade. *Journal of Geophysical Research* 95(D5):5677-5688.

Pearson, E. W., LeBaron, B. A., and J. J. Michalsky. 1988. Decay of the El Chichon perturbation to the stratospheric aerosol layer: multispectral ground-based radiometric observations. *Geophysical Research Letters* 15:24-27.

Rozenberg, G. V. 1966. *Twilight: a study in atmospheric optics*. Plenum Press, New York.

Strahler, A. N. and A. H. Strahler. 1984. *Elements of Physical Geography*, John Wiley & Sons, New York.

Van Heuklon, T. K. 1979. Estimating atmospheric ozone for solar radiation models. *Solar Energy* 22:63-68.

PART 2: INFORMATION ABOUT THE DIGITAL DATA FILES

12. CONTENTS OF THE MAGNETIC MEDIA

The following table describes the 11 files included in this database and distributed by the Carbon Dioxide Information Analysis Center (CDIAC) along with this documentation. These files are available on 8-mm tape, 0.25-in. tape cartridge, IBM-formatted floppy diskettes, and through the Internet via anonymous FTP (at cdiac.esd.ornl.gov) or the World Wide Web (at http://cdiac.esd.ornl.gov/cdiac/).

Table 3. List and description of the digital files.

File number	Name, type, and description	Logical records	Record length	File size (bytes)
1.	NDP053.DOC (ASCII) General descriptive file that contains the information contained in Part 2 of the documentation	517	80	41,360
2.	ALL.FOR (ASCII) FORTRAN retrieval program to read and print files 4 through 11	33	80	2,640
3.	ALL.SAS (ASCII) SAS™ program to read and print files 4 through 11	13	80	1,040
4.	ALLT2.ASC (ASCII) Total optical depths for the 1010 nm, 785 nm, 535 nm, 486 nm, and 428 nm wavelength bands	2,169	51	110,619
5.	ALLT2ERR.ASC (ASCII) Standard error in the Langley determinations of total optical depths for the 1010 nm, 785 nm, 535 nm, 486 nm, and 428 nm wavelength bands	2,169	51	110,619
6	ALLT2S.ASC (ASCII) Smoothed total optical depths for the 1010 nm, 785 nm, 535 nm, 486 nm, and 428 nm wavelength bands	2,169	51	110,619

Table 3. (continued)

File number	Name, type, and description	Logical records	Record length	File size (bytes)
7.	ALLA2.ASC (ASCII) Total column aerosol optical depths for the 1010 nm, 785 nm, 535 nm, 486 nm, and 428 nm wavelength bands	2,169	51	110,619
8.	ALLA2S.ASC (ASCII) Smoothed column aerosol optical depths for the 1010 nm, 785 nm, 535 nm, 486 nm, and 428 nm wavelength bands	2,169	51	110,619
9.	ALLA2R.ASC (ASCII) Residual column aerosol optical depths for the 1010 nm, 785 nm, 535 nm, 486 nm, and 428 nm wavelength bands	2,169	51	110,619
10.	ALLA2RS.ASC (ASCII) Smoothed residual column aerosol optical depths for the 1010 nm, 785 nm, 535 nm, 486 nm, and 428 nm wavelength bands	2,169	51	110,619
11.	BACKGRD.ASC (ASCII) Smoothed background aerosol optical depths for the 1010 nm, 785 nm, 535 nm, 486 nm, and 428 nm wavelength bands	669	51	34,119
	Total records	16,415	Total size	853,492

Note: 1. All files are stored in a fixed-blocked format.
2. SAS™ is a registered trademark of the SAS Institute, Inc., Cary, North Carolina 27511-8000.

13. DESCRIPTIVE FILE ON THE MAGNETIC MEDIA

The following is a listing of the first file provided on the magnetic media distributed by CDIAC. The file provides variable descriptions, formats, units, and other pertinent information about each file associated with this database.

TITLE OF THE DATABASE

Rattlesnake Mountain Observatory (46.4° N, 119.6° W) Multispectral Optical Depth Measurements: 1979–1994

CONTRIBUTORS

Nels R. Larson
Pacific Northwest Laboratory
P.O. Box 999
Richland, Washington 99352-0999
U.S.A.

Joseph J. Michalsky
Atmospheric Sciences Research Center
100 Fuller Road
Albany, New York 12205
U.S.A.

Brock A. LeBaron
Utah Bureau of Air Quality
P.O. Box 16690
Salt Lake City, Utah 84116-0690
U.S.A.

SCOPE OF THE DATA

The numeric data package (NDP) contains measurements of total optical depths for the 428 nm, 486 nm, 535 nm, 785 nm, and 1010 nm wavelength bands; derived total column aerosol optical depths for each band; and smoothed background tropospheric aerosol optical depths. The total optical depth measurements were obtained by a multipurpose photometer installed at the Rattlesnake Mountain Observatory (46.4° N, 119.6° W at an elevation of 1088 m above mean sea) and operated by Pacific Northwest Laboratory (PNL), Richland, Washington.

The mobile automatic scanning photometer (MASP) began operation in March 1979 and has provided continous data since August, 5, 1979. This database contains information from August 5, 1979, to September 2, 1994. Measurements of the attenuation of direct solar radiation are taken by the photometer for different wavelengths using 12 filters. Five of these filters (i.e., those for 428 nm, 486 nm, 535 nm, 785 nm, and 1010 nm wavelengths, with respective half-power widths of 2, 2, 3, 18, and 28 nm) are suitable for monitoring variations

in the total optical depth of the atmosphere.

The measurement routine used to obtain the direct-sun, daytime data samples begins at sunrise and is repeated every 5 minutes until sunset. In each 5 minute sampling period all 12 filters are scanned. This scanning process takes 2-minutes per sampling interval. During the direct Sun measurements the Sun's position is recalculated once per minute to an accuracy of ±0.5°. With the positional accuracy of the instrument of ±0.3° the maximum possible error in pointing the instrument at the Sun is < 1°. To make the direct measurement a sun-centered raster scan is made. Each scan has dimensions of 5.0° in azimuth by 3.0° elevation and generates 110 samples. The largest raster value is then saved.

This sampling process results in the collection of 12 samples per hour for each filter. To determine the total optical depth for each wavelength, the samples taken between air-mass numbers 2 to 6 during cloud free periods in the morning and afternoon are grouped into morning and afternoon observation sets. Thus, the number of sets may vary from 0 to 2 per day, with the number of sample points in each set varying based on the daily change in the Sun's zenith elevation and the presence or absence of clouds.

The data that the researchers used to infer the total atmospheric optical depth for each wavelength are time stamped based on the midpoint of the sampling periods used in each observation set. Because some samples may have been deleted from each 2-to-6 air-mass interval due to clouds, the time stamp associated with each observation set does not simply define the midpoint for the 2 to 6 air-mass interval, but the midtime between the first point and the last point used in calculating the optical depth.

The radiation measurements obtained for each observation set are converted to total optical depths based on the following equation:

$$\tau = \frac{\ln(I_{0\lambda}) - \ln(I_\lambda)}{m} ,$$

where I_λ is the spectral irradiance measured at the surface for wavelength λ, $I_{0\lambda}$ is the spectral irradiance for λ at the top of the atmosphere, m is the equivalent air-mass in the direction of the Sun normalized to the mass of air in the zenith direction (i.e., relative atmospheric path length), and τ is the total optical depth at λ in the zenith direction.

The spectral irradiance at the surface is directly measured by the MASP, irradiance at the top of the atmosphere is derived based on Langley regression, and m is the relative path length (air-mass number) of the samples used in the observational set and is derived from Rozenberg's formula relating solar zenith angle to air-mass. This equation provides a more accurate air-mass value than the simple geometrical relation where air-mass is the secant of the zenith angle. In this database, only samples taken between air-mass numbers 2 and 6 have been used; this converts to time periods when the Sun is ~30° to 9.3° above the horizon.

To determine the value of $\ln(I_{0\lambda})$ and τ for each wavelength, a plot of $\ln(I_\lambda)$ vs m was made from the data samples in each observation set, and a Langley regression performed. The intercept and slope of the regression line are $\ln(I_{0\lambda})$ and τ, respectively. The value of τ at λ comprises four components and may be written as:

$$\tau = \tau_a + \tau_o + \tau_m + \tau_R ,$$

where the subscripts denote aerosol, ozone, molecular, and Rayleigh optical depths. Values for τ_o, τ_m, and τ_R are known and can be subtracted from τ, leaving us with the total column aerosol optical depth for each wavelength. Values for τ_o and τ_R were calculated based on the work of Van Heuklon, and Hansen and Travis, respectively, and the contribution of τ_m was assumed to be zero since the five filters were selected to avoid virtually all forms of molecular absorption with the exception of aerosols. The calculated Rayleigh optical depths are 0.007311, 0.020183, 0.095607, 0.141625, and 0.238906 for the 1010 nm, 785 nm, 535 nm, 486 nm, and 428 nm filters, respectively.

After the total column aerosol optical depth was determined for each band, it was partitioned into tropospheric and stratospheric components. The procedure for separating the total aerosol optical depth into its components is based on the assumption that the aerosol optical depth of the troposphere, though highly variable, has a predictable underlying seasonal behavior. The background aerosol data were derived from measurements taken during periods of low stratospheric loading from June 15, 1987, to June 15, 1991, inclusive, folded into a single year. The "year" was then smoothed using a locally weighted regression method. By removing this seasonal behavior from τ_a, a residual aerosol optical depth was derived that was assumed to be the contribution from the stratosphere.

Thus, the equations described above were used to convert solar irradiance measurements taken at the surface to total optical depths for each wavelength. These total optical depths were then corrected for ozone and Rayleigh scattering and total column aerosol optical depths obtained. The estimated background aerosol optical depths were then subtracted from τ_a to obtain the residual (estimated stratospheric) aerosol optical depth for each wavelength.

FILE DESCRIPTIONS

The data were initially received in flat ASCII files and required minimal reformatting. This NDP consists of 1 flat ASCII documentation file, 1 SAS™ program, 1 FORTRAN program, and 8 ASCII data files, for a total of 11 digital files. The flat ASCII documentation file (NDP053.DOC) contains most of the information contained in Part 2 of this document, with postscript graphics and special control characters and graphic symbols removed. The SAS™ and FORTRAN files (ALL.SAS and ALL.FOR) are in ASCII formats and contain programs to read and print the flat ASCII data files. The eight ASCII data files contain, for five wavelengths, total optical depths (ALLT2.ASC), the standard error of the Langley determination of the total optical depths (ALLT2ERR.ASC), smoothed total optical depths (ALLT2S.ASC), total aerosol optical depths (ALLA2.ASC), smoothed aerosol optical depths (ALLA2S.ASC), estimated background aerosol optical depths (BACKGRD.ASC), residual aerosol optical depths (ALLA2R.ASC), and smoothed residual aerosol optical depths (ALLA2RS.ASC).

FILE FORMATS

The data in the data files were derived directly from the total optical depths calculated from the MASP measurement and were derived in the following order: ALLT2.ASC, ALLT2ERR.ASC, and ALLT2S.ASC. The aerosol optical depth files were derived from ALLT2.ASC as follows: ALLA2.ASC and ALLA2S.ASC. File BACKGRD.ASC was then

subtracted from ALLA2.ASC to obtain ALLA2R.ASC and ALLA2RS.ASC (these files are estimates of the stratospheric aerosol optical depth).

All eight data files are formatted in the same manner. The FORTRAN and SAS™ programs (ALL.FOR and ALL.SAS) provided with this NDP allow the user to read and print, with minimal modification, the contents of each data file. A summary of the FORTRAN statements used to read the data follows:

```
      REAL YEAR, NM1010, NM785, NM535, NM486, NM428
 10   READ (5,100,END=999) YEAR, NM1010, NM785, NM535,
    1                       NM486, NM428
      GOTO 10
C
 100  FORMAT(F10.5,5F8.4)
```

Table 4 provides a listing of the variables contained in each data file. The variable formats are identical for all eight ASCII data files.

Table 4. Variable formats for the eight flat ASCII data files.

Variable name	Variable type	Variable width	Column Start	Column End	Variable description
YEAR	Real	10	1	10	Time stamp for each observational set. Values are in year.fraction format. Values accurate to 1 minute.
NM1010	Real	8	11	18	Data for the 1010-nm wavelength filter.
NM785	Real	8	19	26	Data for the 785-nm wavelength filter.
NM535	Real	8	27	34	Data for the 535-nm wavelength filter.
NM486	Real	8	35	42	Data for the 486-nm wavelength filter.
NM428	Real	8	43	50	Data for the 428-nm wavelength filter.

14. LISTING OF THE FORTRAN AND SAS™ DATA RETRIEVAL PROGRAMS

This section lists the FORTRAN and SAS™ programs provided by CDIAC to read and print the contents of the ASCII data files. The two programs shown below (ALL.FOR and ALL.SAS) have been designed to be used with all eight ASCII data files with minimal modification (i.e., changing the name of the input file).

ALL.FOR

```
C*********************************************************
C*   FORTRAN PROGRAM TO READ AND PRINT FILES ALLT2.ASC,  *
C*   ALLT2ERR.ASC, ALLT2S.ASC, ALLA2.ASC, ALLA2S.ASC,    *
C*   ALLA2R.ASC, ALLA2RS.ASC, AND BACKGRD.ASC.           *
C*********************************************************

        REAL YEAR, NM1010, NM785, NM535, NM486, NM428

C*********************************************************
C*   OPEN FILES FOR INPUT/OUTPUT                         *
C*********************************************************
        OPEN(UNIT=5,FILE='allt2.asc')
        OPEN(UNIT=6,FORM='PRINT')

C*********************************************************
C*   READ AND PRINT YEAR.FRACTION AND TOTAL OPTICAL OR   *
C*   AEROSOL DEPTHS FOR 5 WAVELENGTHS.                   *
C*********************************************************
  10    READ (5,100,END=999) YEAR, NM1010, NM785, NM535,
     1                         NM486, NM428
        WRITE(6,110) YEAR, NM1010,  NM785, NM535,
     1                         NM486, NM428
        GOTO 10
C

 100    FORMAT(F10.5,5F8.4)
 110    FORMAT(1X,F10.5,5F8.4)

C*********************************************************
C*          CLOSE FILES AND EXIT GRACEFULLY              *
C*********************************************************
 999    CLOSE(UNIT=5)
        CLOSE(UNIT=6)
        STOP
        END
```

ALL.SAS

```
/*
  THIS PROGRAM READS AND PRINTS THE CONTENTS
  OF FILE ALLT2.ASC. CHANGE INFILE NAME TO
  PRINT FILES ALLT2ERR.ASC, ALLT2S.ASC, ALLA2.ASC,
  ALLA2S.ASC, ALLA2R.ASC, ALLA2RS.ASC, AND BACKGRD.ASC
*/
OPTIONS LS=75 PS=65;
DATA DEPTH;
INFILE './allt2.asc';
INPUT YEAR 10.5 NM1010 NM785 NM535 NM486 NM428;
PROC PRINT NOOBS;
     FORMAT YEAR 10.5;
RUN;
```

15. VERIFICATION OF DATA TRANSPORT

After the data files provided with this NDP are loaded onto a system, or downloaded from CDIAC's anonymous FTP area, the user should check to verify that the files have not been corrupted in transport. This may be done by generating some or all of the statistics presented in Table 5. These statistics are included as a tool to ensure proper reading of the eight ASCII data files and should not be construed as either a summary or an indicator of trends in the data.

These statistics were obtained using the SAS™ software package with the PROC MEANS procedure. These statistics may be duplicated using other statistical packages or computer languages.

Table 5. Statistical characteristics of the numeric variables in the eight ASCII data files.

File name / Variable	N	Mean	Std. Dev.	Minimum	Maximum
ALLT2.ASC					
YEAR	2169	1987.35	4.1857731	1979.59	1994.67
NM1010	2169	0.0521685	0.0339624	0.0030000	0.2395000
NM785	2169	0.0793119	0.0406188	0.0180000	0.2735000
NM535	2169	0.1941314	0.0487121	0.1129000	0.5257000
NM486	2169	0.2299527	0.0525812	0.1351000	0.6386000
NM428	2169	0.3402344	0.0607183	0.2359000	0.8001000

Table 5. (continued)

File name Variable	N	Mean	Std. Dev.	Minimum	Maximum
ALLT2ERR.ASC					
YEAR	2169	1987.35	4.1857731	1979.59	1994.67
NM1010	2169	0.0031233	0.0016285	0.0006000	0.0158000
NM785	2169	0.0031494	0.0016306	0.0008000	0.0148000
NM535	2169	0.0035638	0.0022722	0.0009000	0.0250000
NM486	2169	0.0042135	0.0025279	0.0013000	0.0235000
NM428	2169	0.0071237	0.0037278	0.0018000	0.0282000
ALLT2S.ASC					
YEAR	2169	1987.35	4.1857738	1979.59	1994.67
NM1010	2169	0.0497653	0.0288188	0.0144000	0.1746000
NM785	2169	0.0767928	0.0349821	0.0333000	0.2336000
NM535	2169	0.1895863	0.0354300	0.1303000	0.3359000
NM486	2169	0.2242478	0.0359460	0.1594000	0.3724000
NM428	2169	0.3330098	0.0385482	0.2558000	0.4898000
ALLA2.ASC					
YEAR	2169	1987.35	4.1857731	1979.59	1994.67
NM1010	2169	0.0448626	0.0339549	0	0.2321000
NM785	2169	0.0566324	0.0405648	0	0.2506000
NM535	2169	0.0727139	0.0482412	0	0.4056000
NM486	2169	0.0806623	0.0524418	0	0.4897000
NM428	2169	0.1012282	0.0607150	0	0.5611000
ALLA2S.ASC					
YEAR	2169	1987.35	4.1857738	1979.59	1994.67
NM1010	2169	0.0424707	0.0288216	0.0072000	0.1700000
NM785	2169	0.0541236	0.0349194	0.0107000	0.2086000
NM535	2169	0.0681527	0.0348450	0.0100000	0.2098000
NM486	2169	0.0749053	0.0357201	0.0109000	0.2163000
NM428	2169	0.0939047	0.0384982	0.0185000	0.2492000
ALLA2R.ASC					
YEAR	2169	1987.35	4.1857731	1979.59	1994.67
NM1010	2169	0.0191247	0.0325577	-0.0278000	0.2020000
NM785	2169	0.0240145	0.0388352	-0.0324000	0.2150000
NM535	2169	0.0291336	0.0457584	-0.0472000	0.3644000
NM486	2169	0.0317047	0.0498039	-0.0652000	0.4421000
NM428	2169	0.0352311	0.0577417	-0.0693000	0.4967000

Table 5. (continued)

File name Variable	N	Mean	Std. Dev.	Minimum	Maximum
ALLA2RS.ASC					
YEAR	2169	1987.35	4.1857738	1979.59	1994.67
NM1010	2169	0.0167009	0.0275359	-0.0111000	0.1360000
NM785	2169	0.0214135	0.0333040	-0.0092000	0.1674000
NM535	2169	0.0244740	0.0322253	-0.0142000	0.1537000
NM486	2169	0.0259101	0.0328810	-0.0168000	0.1498000
NM428	2169	0.0278258	0.0352972	-0.0275000	0.1628000
BACKGRD.ASC					
YEAR	669	0.5282713	0.2324004	-0.0030100	1.0047300
NM1010	669	0.0248658	0.0069869	0.0091000	0.0374000
NM785	669	0.0315368	0.0086413	0.0129000	0.0485000
NM535	669	0.0420392	0.0117443	0.0168000	0.0652000
NM486	669	0.0471555	0.0134666	0.0167000	0.0707000
NM428	669	0.0640024	0.0150460	0.0276000	0.0867000

The following listings contain the first five and last five lines in each of the eight ASCII data files.

Sample listing from ALLT2.ASC

```
1979.59347 0.0226 0.0424 0.1520 0.1799 0.2858
1979.59470 0.0337 0.0648 0.1897 0.2343 0.3473
1979.59741 0.0351 0.0532 0.1560 0.1962 0.2850
1979.60018 0.0407 0.0574 0.1514 0.1798 0.2800
1979.60169 0.0286 0.0550 0.1735 0.2130 0.3121
...
1994.63026 0.0434 0.0652 0.1772 0.2132 0.3303
1994.63185 0.0951 0.1306 0.2854 0.3342 0.4708
1994.63301 0.0267 0.0551 0.1660 0.2039 0.3024
1994.66583 0.0756 0.1166 0.2703 0.3211 0.4475
1994.66749 0.0683 0.1007 0.2352 0.2841 0.4043
```

Sample listing from ALLT2ERR.ASC

1979.59347	0.0025	0.0025	0.0071	0.0067	0.0069
1979.59470	0.0033	0.0027	0.0061	0.0129	0.0057
1979.59741	0.0033	0.0025	0.0074	0.0109	0.0095
1979.60018	0.0042	0.0038	0.0049	0.0056	0.0040
1979.60169	0.0029	0.0031	0.0095	0.0100	0.0132
...					
1994.63026	0.0023	0.0035	0.0027	0.0040	0.0087
1994.63185	0.0027	0.0025	0.0025	0.0040	0.0127
1994.63301	0.0028	0.0044	0.0037	0.0045	0.0128
1994.66583	0.0052	0.0061	0.0023	0.0061	0.0111
1994.66749	0.0020	0.0025	0.0031	0.0033	0.0113

Sample listing from ALLT2S.ASC

1979.59351	0.0336	0.0576	0.1656	0.2031	0.3074
1979.59473	0.0335	0.0578	0.1680	0.2020	0.3059
1979.59741	0.0336	0.0573	0.1666	0.2023	0.3053
1979.60022	0.0334	0.0582	0.1687	0.2017	0.3073
1979.60168	0.0334	0.0575	0.1686	0.2029	0.3027
...					
1994.63025	0.0557	0.0890	0.2220	0.2657	0.3807
1994.63184	0.0558	0.0895	0.2235	0.2656	0.3848
1994.63306	0.0560	0.0897	0.2237	0.2673	0.3835
1994.66577	0.0607	0.0965	0.2369	0.2846	0.4006
1994.66748	0.0616	0.0975	0.2385	0.2836	0.4015

Sample listing from ALLA2.ASC

1979.59347	0.0153	0.0197	0.0308	0.0307	0.0468
1979.59470	0.0264	0.0421	0.0686	0.0851	0.1083
1979.59741	0.0278	0.0306	0.0349	0.0470	0.0460
1979.60018	0.0334	0.0348	0.0303	0.0306	0.0410
1979.60169	0.0213	0.0324	0.0525	0.0638	0.0731
...					
1994.63026	0.0361	0.0426	0.0565	0.0641	0.0913
1994.63185	0.0878	0.1080	0.1647	0.1851	0.2318
1994.63301	0.0193	0.0324	0.0454	0.0548	0.0633
1994.66583	0.0683	0.0941	0.1501	0.1721	0.2085
1994.66749	0.0610	0.0781	0.1150	0.1352	0.1653

Sample listing from ALLA2S.ASC

1979.59351	0.0265	0.0355	0.0461	0.0541	0.0664
1979.59473	0.0262	0.0351	0.0460	0.0545	0.0655
1979.59741	0.0264	0.0350	0.0458	0.0541	0.0656
1979.60022	0.0263	0.0348	0.0461	0.0536	0.0663
1979.60168	0.0263	0.0349	0.0458	0.0539	0.0669
...					
1994.63025	0.0483	0.0663	0.1011	0.1160	0.1434
1994.63184	0.0488	0.0667	0.1017	0.1166	0.1443
1994.63306	0.0490	0.0668	0.1025	0.1180	0.1448
1994.66577	0.0538	0.0740	0.1155	0.1351	0.1634
1994.66748	0.0541	0.0743	0.1159	0.1356	0.1666

Sample listing from ALLA2R.ASC

1979.59347	-0.0126	-0.0152	-0.0188	-0.0265	-0.0280
1979.59470	-0.0015	0.0072	0.0189	0.0280	0.0337
1979.59741	0.0000	-0.0045	-0.0148	-0.0100	-0.0286
1979.60018	0.0057	-0.0004	-0.0195	-0.0263	-0.0337
1979.60169	-0.0063	-0.0028	0.0026	0.0069	-0.0017
...					
1994.63026	0.0112	0.0104	0.0104	0.0118	0.0198
1994.63185	0.0629	0.0759	0.1187	0.1328	0.1602
1994.63301	-0.0055	0.0004	-0.0006	0.0026	-0.0083
1994.66583	0.0432	0.0628	0.1067	0.1221	0.1396
1994.66749	0.0359	0.0470	0.0719	0.0856	0.0972

Sample listing from ALLA2RS.ASC

1979.59351	-0.0020	-0.0005	-0.0040	-0.0036	-0.0089
1979.59473	-0.0019	-0.0004	-0.0039	-0.0035	-0.0087
1979.59741	-0.0019	-0.0003	-0.0037	-0.0033	-0.0085
1979.60022	-0.0018	-0.0003	-0.0034	-0.0031	-0.0082
1979.60168	-0.0017	-0.0002	-0.0033	-0.0030	-0.0081
...					
1994.63025	0.0223	0.0331	0.0547	0.0634	0.0714
1994.63184	0.0227	0.0334	0.0555	0.0639	0.0728
1994.63306	0.0227	0.0336	0.0561	0.0644	0.0727
1994.66577	0.0276	0.0416	0.0691	0.0815	0.0924
1994.66748	0.0284	0.0420	0.0705	0.0821	0.0931

Sample listing from BACKGRD.ASC

-0.00301	0.0094	0.0131	0.0177	0.0175	0.0285
0.00473	0.0095	0.0132	0.0180	0.0178	0.0288
0.03267	0.0103	0.0140	0.0197	0.0191	0.0308
0.04024	0.0104	0.0141	0.0202	0.0194	0.0312
0.04087	0.0104	0.0141	0.0202	0.0195	0.0313
...					
0.97744	0.0091	0.0129	0.0170	0.0169	0.0278
0.98564	0.0092	0.0130	0.0173	0.0172	0.0281
0.98608	0.0092	0.0130	0.0173	0.0172	0.0281
0.99699	0.0094	0.0131	0.0177	0.0175	0.0285
1.00473	0.0095	0.0132	0.0180	0.0178	0.0288

APPENDIX: PERTINENT LITERATURE

OTHER SUGGESTED READING:

Radiometric characterization of Mount Pinatubo's stratospheric aerosols over northern mid-latitudes. By N. R. Larson and J. J. Michalsky. Submitted to the *Journal of Geophysical Research* for publication in 1996.

Reprinted with permission

J. J. Michalsky, E. W. Pearson, and B. A. LeBaron. Journal of Geophysical Research, Volume 95(D5):5677-5688, copyright by the American Geophysical Union.

JOURNAL OF GEOPHYSICAL RESEARCH, VOL. 95, NO. D5, PAGES 5677-5688, APRIL 20, 1990

AN ASSESSMENT OF THE IMPACT OF VOLCANIC ERUPTIONS ON THE NORTHERN HEMISPHERE'S AEROSOL BURDEN DURING THE LAST DECADE

J. J. Michalsky

Atmospheric Sciences Research Center, State University of New York at Albany

E. W. Pearson and B. A. LeBaron

Pacific Northwest Laboratory, Richland, Washington

Abstract. We present an analysis of volcanic aerosol loading above a northern mid-latitude observing station during the last decade, with particular attention to the decay in the aerosol resulting from the 1982 eruption of El Chichon. The optical depth data at five wavelengths are derived from sunradiometry data. These are tabulated, and inferences regarding size distribution of the volcanic aerosol are drawn. Comparison with a number of other data sets is used to establish the validity of our ground-based technique, and to draw inferences regarding stratospheric transport. We also report simulation calculations designed to establish the capabilities and limitations of our measurement and analysis techniques. The main conclusions of the study are as follows. Under suitable conditions, ground-based sunradiometry can reliably monitor variations in the stratospheric aerosol of less than 0.01 optical depths on time scales of a few weeks or longer. Large (on the order of 0.5 micrometer) particles remained present throughout the decay of the El Chichon aerosol, and there is substantial agreement among mid-latitude data sets collected by several techniques; thus inferences regarding stratospheric transport can be drawn from joint analysis of the available data. The available evidence supports the proposition that mid-latitude decay is modulated by annual transport of fresh material from low latitudes, primarily, with some transport from polar latitudes.

1. Introduction

The past 10 years have been a particularly auspicious period for the study of volcanic perturbations of the atmosphere. The early part of this decade was noteworthy because the stratosphere was extremely clean, with no eruptions since Fuego in 1974 contributing substantially to the stratospheric layer [Hofmann and Rosen, 1981]. From the perspective of observers in the northern mid-latitudes, three successively larger volcanic events then followed beginning in May 1980 with the eruption of St. Helens in Washington State. This was followed less than a year later in April 1981 with a larger stratospheric perturbation by Alaid in the Kurile Islands off the Kamchatka Peninsula of Asia. A "mystery cloud" appeared in lidar profiles in early 1982 [Hirono and Shibata, 1983], but it was completely masked when El Chichon erupted in April 1982 to produce the largest aerosol perturbation to the stratosphere in the last century.

Copyright 1990 by the American Geophysical Union.

Paper number 89JD03111.
0148-0227/90/89JD-03111$05.00

A quiescent period of three and one-half years followed, allowing researchers to observe the decay of that perturbation. This period was interrupted in November 1985 by the eruption of Ruiz in Columbia.

El Chichon was the most significant source of stratospheric aerosol since Krakatau in 1883. It is by far the most thoroughly studied volcano to date, although the investigation of the global impact was noticeably impaired by the absence of an operational SAGE satellite [Mauldin et al., 1985] during the eruption and early decay. This could have provided pole-to-pole measurements of the transport and evolution of the aerosol cloud. Hofmann [1987] reviewed the published information on the El Chichon aerosol through 1985.

El Chichon erupted three times on March 28, April 3, and April 4, 1982 [Rampino and Self, 1984]. According to Hofmann [1987], the first two eruptions did not penetrate the 22-km level that separated easterly and westerly flow aloft. The final eruption deposited about 90% of the total atmospheric mass of the three eruptions above this altitude. The westerly flow below 22 km moved the lesser debris northward during the spring and summer. The bulk of the higher altitude aerosol was confined to latitudes below 30°N until some six months later. The stratospheric loading for northern mid-latitudes reached a peak around late winter-early spring nearly a full year after the eruptions. While the decay in loading from the peak was generally exponential, enhancements were clearly identified during the winters of 1984 and 1985.

In this paper we analyze a continuous data set of multispectral optical depth measurements made from the ground covering the period 1978-1988. This analysis differs from others in that the total aerosol column background and perturbation are separated. In the following section a brief description of the process followed and errors associated with estimating volcanic aerosol perturbations using ground-based sunradiometry is presented. In the third section basic results using our technique, including a description of the mid-latitude peaking and recovery are described. Optical depth data at five wavelengths are used to infer aerosol size changes during the decade. In section 4 results are compared with other northern hemisphere measurements of stratospheric loading, first, as a means of validating the ground-based method and, second, to investigate the transport of stratospheric mass. The final section closes with a comparison of the merits of our ground-based technique with those of other ground-based methods, and with sampling procedures that measure stratospheric aerosol only. Our understanding regarding transport in the lower stratosphere in light of this study is summarized. Appendices contain a brief explanation of our measurements and optical depth calculations, quarter-year estimates of aerosol optical depth for the stratosphere as calculated by

our procedure, and some details of the estimation process and the calculation of error bounds.

2. Volcanic Aerosol Measurement by Sunradiometry

To obtain the results presented in this paper, we have analyzed a 10-year time series of total column aerosol optical depth data at five wavelengths (428, 486, 535, 785, and 1010 nm). This data set has been derived through reduction of sunradiometry data taken at our Rattlesnake Mountain Observatory (altitude, 1085 m; latitude, 46.4°N; longitude, 119.6°W) from 1978 to 1988. The instrument and data reduction procedures have been described elsewhere [Kleckner et al., 1981; Michalsky and Stokes, 1983; Pearson et al., 1988]; this material is briefly summarized in Appendix A.

Our aerosol optical depth data are for the total column above the observing site. To calculate stratospheric loading, it is necessary to decompose the total column optical depth into its tropospheric and stratospheric components,

$$t_{aer} = t_{trop} + t_{strat}$$

These two components have quite different characteristics. The tropospheric component, t_{trop}, is highly variable on time scales of hours or days, and is dominant during periods of low stratospheric loading. t_{strat} is not affected by synoptic conditions, and is comparable in magnitude to t_{trop} only in the months immediately following a major volcanic perturbation.

Our procedure for separating t_{aer} into its components is based on the fundamental assumption that t_{trop}, although noisy on short time scales, has an underlying seasonal behavior that does not change significantly from year to year. Analysis of a 28-year time series of pyrheliometric data collected at Tucson [Szymber and Sellers, 1985] and our own observations indicate that this assumption is reasonable in the current application. The decomposition procedure has several steps. We begin by inferring the seasonally varying tropospheric background at each wavelength as a smoothed average of data collected during periods of low stratospheric loading folded onto a single year (details in Appendix A). The full optical depth time series is then differenced against the background, and the result smoothed as well. This smoothed difference time series is our estimate of the perturbation from the background of the aerosol optical depth at our observing site.

Before discussing the results, there are a few points we wish to emphasize. First, because of the high short-term variability in optical depth, it is necessary to use a smoothing technique that is resistant to outliers. We use a locally weighted resistant regression method developed by Cleveland [1979]. Second, although we refer to our decomposition as yielding tropospheric and stratospheric components, it is more accurate to describe these components as background and perturbation, respectively. There is a modest stratospheric contribution to the background, and, in the early stages, there may be some tropospheric contribution to the perturbation. Finally, we note that, because of the smoothing, the heights of the sharp peaks will be underestimated. Consequently, we do not expect the method described here to necessarily yield accurate values for the peak loading if the peak is of very short duration.

Figure 1 is a plot of the difference data and smoothed fit to that data for 785 nm. The names of the volcanoes are printed above their stratospheric effect. St. Helens is a minor contributor of stratospheric aerosol. Alaid has a somewhat larger effect, El Chichon is an order of magnitude larger, and Ruiz renders uncertain the further decay of El Chichon aerosols. Other prominent features in this plot are the secondary maxima in the winter of 1984 and in the winter of 1985.

Our approach to estimating the uncertainty in the inferred El Chichon optical depths is described in detail in Appendix B. In addition to comparison with the results of other investigators (section 4) we have carried out a suite of simple Monte Carlo simulations to test the entire analysis procedure, and have applied the "jacknife" resampling technique [Efron, 1982] to obtain confidence intervals for our results. Briefly, the results demonstrate that, given the measurement frequencies obtained in this work and our underlying assumptions regarding temporal variability in the background aerosol, the ground-based technique can detect stratospheric perturbations of reasonable duration on the order of 0.01 optical depths or less. Ninety percent confidence intervals are displayed in Figure 2.

3. Basic Results

Figure 3 presents the smoothed estimates of volcanic perturbations at each of the five wavelengths. It is clear that the eruptions identified in Figure 1 are confirmed at the other four wavelengths, although there are significant differences in the strengths of the perturbations. The amplitudes of the secondary maxima that occur each of two winters after El Chichon peaks in 1983 are enhanced at the shortest wavelength. If we measure the decay time from each of the three peaks, we find that the optical depth reaches 1/eth of its peak value in about 200 days. This

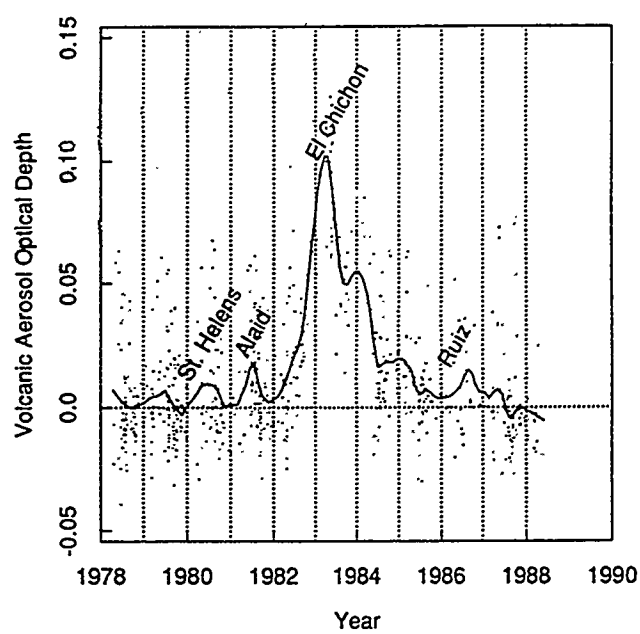

Fig. 1. Smoothed estimate of the time-dependent volcanic optical depth perturbation to the atmosphere at 785 nm. Volcano names are to be associated with their atmospheric effects.

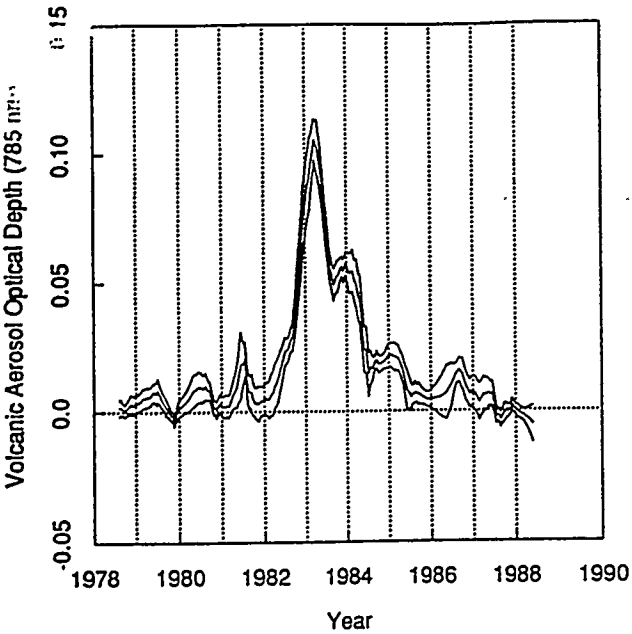

Fig. 2. Time series estimate of volcanic aerosol perturbation at 785 nm and the 90% confidence intervals for our estimate.

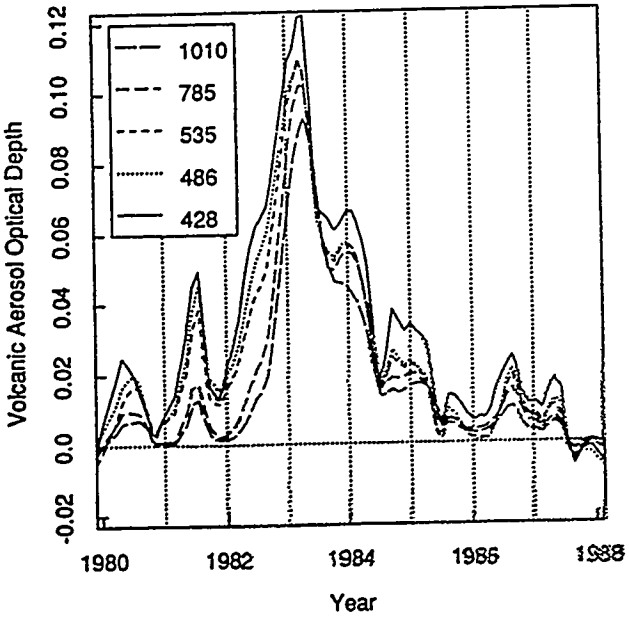

Fig. 3. Time series estimate of volcanic aerosol loading after background subtracted for the five PNL sunradiometer wavelengths.

rapid decay is much shorter than the 12-month decay rate calculated using the peak mixing ratio data of Hofmann [1987], however, it agrees with Post's [1984] infrared lidar measurement of total integrated backscatter at 10.6 micrometers. All perturbations are maximal at the shortest wavelength. Alaid's effect is much more pronounced in the blue than it is in the near-infrared. At the El Chichon peak, on the other hand, there is a much smaller gradient with wavelength than there is for Alaid. The evolution from a large to a small gradient is observed throughout 1982 with the influence of El Chichon very strong initially only at the shortest wavelengths. To examine what this implies with regard to particle size evolution, we use a standard approach in sunradiometry.

Junge [1963] showed that a power law size distribution, which is often approximated in urban and continental air masses, leads to a wavelength dependence expressed as

$$\tau = \beta\lambda^{-\alpha} \tag{1}$$

where τ is the optical depth, β is a constant related to total aerosol load, and α is the size parameter. For very small particles, α approaches 4, i.e., Rayleigh scattering. If the particles are much larger than the wavelength, α is nearly zero. Even though the power law distribution does not describe the physical distribution of particle sizes exactly, this procedure is a useful qualitative indicator of size distribution. Figure 4 is a smoothed plot of α obtained from the slope of the linear least squares fit of the log-log plot of the variables in (1). Aerosol optical depth data are the smoothed total column values for this calculation, i.e., the tropospheric aerosol is included. The linear correlation coefficient between $\log(\tau)$ and $\log(\lambda)$ was above 0.95 in all cases. There is an irregular variation in α before the Alaid eruption and a general trend to larger α, i.e., smaller particles, until 1982. El Chichon had a dramatic impact on the mean particle size in the total column. At peak loading, α dropped to about 0.4 implying a substantial increase in large particles. (Although α variations could reflect composition changes, King et al. [1984] point out that El Chichon aerosol has nearly the same composition as the background stratosphere.) This large particle increase was also reported by other investigators sampling at mid-latitudes [e.g., Hofmann

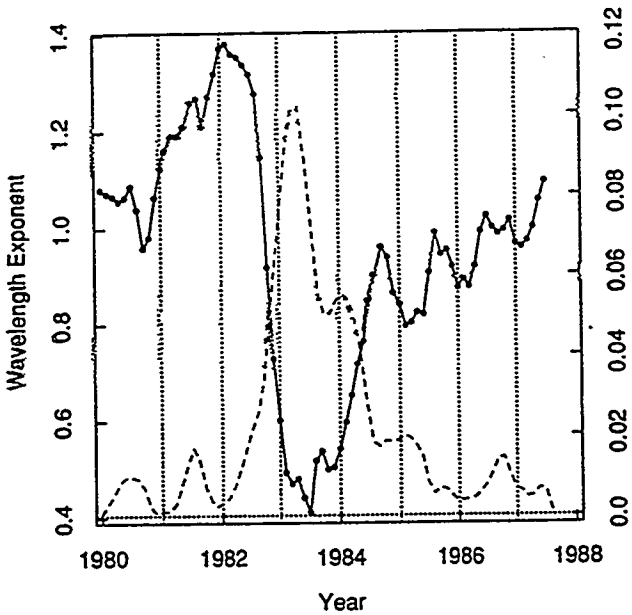

Fig. 4. Time series plot of wavelength dependence parameter, α, from (1). Small values imply large particles. Also plotted is the smoothed estimate of the 785-nm differenced data of Figure 1. This is intended to facilitate the comparison of some features of the plot with stratospheric events.

and Rosen, 1984; Spinhirne and King, 1985]. As the El Chichon layer decayed, α slowly returned to pre-eruption values, but superimposed on the slow increase in α is an apparent shift to larger particles each winter, beginning in 1985. Such an increase could, at least, partially account for the wintertime maxima of 1984 and 1985 in the El Chichon decay. However, this interpretation is not consistent with the wavelength dependence of the El Chichon perturbation (Figure 3). Compare the summers of 1983 and 1984 with the winters that follow: in both cases the shorter wavelengths are dominant during the cold months rather than the warm months implying just the opposite behavior, i.e., the volcanic particles are actually larger in the summertime for the perturbed atmosphere. The increase in particle size that is repeated during the winters of 1985, 1986, and 1987, after a substantial decrease in El Chichon aerosol, is consistent with the study of Brogniez and Lenoble [1987], who found that for the volcanically undisturbed stratosphere, aerosol size and optical depth increase in the winter months. Since Figure 4 is based on total column measurements, we are not able to exclude a size increase in tropospheric aerosol during the winter months as part of the explanation of these latter features however.

In Figure 5 the optical depths, representing the volcanic burden 6 months before, during, and 6 months after the peak loading at mid-latitudes, are inverted using the King et al. [1978] algorithm to examine the change in size distribution. The bulk of the stratospheric mass began its movement north in the early fall of 1982. The size distribution in Figure 5a clearly follows a power law. This represents the early fall arrival of smaller particles than were present at the peak as is indicated in Figure 20 of Hofmann [1987]. The size distribution during our peak loading around March 1983 is illustrated in Figure 5b. It appears to have an intermediate size distribution between that of October/November 1982 and May 1983, as indicated in Spinhirne and King [1985], for roughly the same latitude. In Figure 5c, as the volcanic load begins to decay around July 1983, the large particle component becomes even more pronounced with a size distribution of similar shape to that of Spinhirne and King's May 1983 data, but with a peak at larger radii. This apparent shift in peak may simply reflect the error associated with the inversion of extinction data.

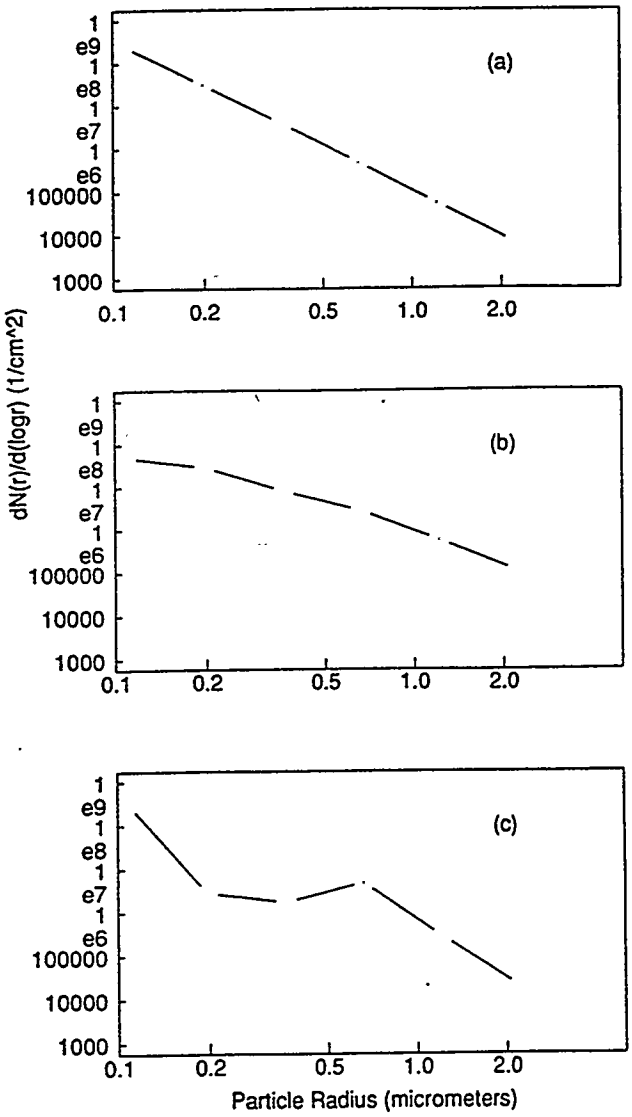

Fig. 5. Volcanic aerosol size distributions based on mathematical inversion of optical depth data (a) six months before, (b) during, and (c) six months after the peak volcanic load.

4. Comparison With Long-Term Data Bases

In this section we compare our results with those obtained by other investigators. The comparisons have two purposes: we wish to corroborate our findings with those of others at similar latitudes, and we hope to investigate the transport of aerosol by comparing total loading at other latitude sites. The most useful data for this intercomparison are those observations of vertically integrated stratospheric aerosol burden that include the pre-eruption period and continue throughout the eruption and decay of El Chichon. The lidar data from Langley Research Center (provided by M.P. McCormick), from the Fraunhofer-Institute for Atmospheric Environmental Research at Garmisch-Partenkirchen (GP) [Jager, 1987a,b], and from the Mauna Loa Observatory [DeLuisi et al., 1985, 1986]; the SAM II satellite data [McCormick and Trepte, 1987], and the data reported here are the routine measurements of the total stratospheric aerosol burden during this period. Table 1 contains a description of the data sets used in this intercomparison.

For comparison purposes we have converted each of these data sets to aerosol optical depth at 694.3 nm. The backscatter-to-extinction time-dependent function of Jager [1987b] was used to convert the mid-latitude lidar data to optical depths. The Mauna Loa integrated backscatter data were converted to optical depths using a constant multiplicative factor of 45 [Deluisi et al., 1989]. The time-averaged wavelength dependence of the sunradiometer volcanic aerosol optical depth for the 1982-1985 period is used to adjust the 1000-nm satellite optical depths and the 785-nm sunradiometer optical depths to 694.3 nm using linear interpolation.

Since the observations are made at different latitudes and may sample different size distributions, there is uncertainty in the backscatter to optical depth conversion process, and there may be some error in using linear interpolation between wavelengths. The integration to get stratospheric column optical depths begins at slightly different heights above the troposphere for the different data sets. Despite these

TABLE 1. Northern Hemisphere Volcanic Aerosol Data Sets

Site	Method	λ, nm	Location	Measurements/day
GP	Lidar B_{scat} (trop + 1 km)	694.3	47.5°N,11.0°E	1/10
Langley	Lidar B_{scat}	694.3	37.0°N,76.0°W	1/20
SAM II	Limb extinct (trop + 2 km)	1000	64 to 82°N	14
Mauna Loa	Lidar B_{scat} (trop)	694.3	19.5°N,155.6°W	1/13
PNL	Differential Sun radiometry	428,486,535 785,1010	46.4°N,119.6°W	1/2.5

uncertainties and differences, transformation of the data sets to a single wavelength is necessary for meaningful comparisons.

In Figure 6 three mid-latitude data sets are plotted. The sites are at northern latitudes of 37°(Langley), 46.4°(PNL), and 47.5°(GP). Each data set has been smoothed using the technique described in section 2. This smoothing was implemented to concentrate on the main features of the time series plots. The three mid-latitude sites show similar behavior, but differ in some details. The largest fractional differences are found at low amplitudes (less than 0.01 in optical depth). These sites all indicate increases after the eruption of St. Helens in 1980, but the amplitude is only about 0.01 optical depth. All three indicate a larger effect following the Alaid eruption with similar amplitudes in optical depth. All three mid-latitude sites reached peak loading from El Chichon within a month or two, almost a year after the low-latitude eruption. The difference in magnitude may be caused by the uncertainty in the techniques and the transformations, or the difference could be real. During the subsequent decay, the data sets exhibit wintertime maxima although each have slightly different amplitudes. Ruiz erupted in November 1985, thus obfuscating the decay of El Chichon.

Figure 7 provides a more detailed comparison of PNL and GP data. The sites are very near in latitude (46.4°N and 47.5°N, respectively). The differences are generally small (less than 0.01 optical depths), except around the two highest peaks. The difference could be partially attributed to the conversion of lidar backscattering to extinction, errors in the ground-based differencing technique, or the interpolation of 785-nm optical depths to 694.3 nm. As discussed in Appendix B, some of the difference in the peak estimate may be associated with the smoothing procedure. It seems plausible, however, to assign much of the discrepancy to fundamental differences in the measurement techniques. GP data are integrated values from the tropopause plus 1 km to the lidar ceiling, which is above virtually all of the aerosol. The PNL ground-based method attempts to zero the background optical depth, even though a portion of this background is stratospheric. Presumably one would be very near the GP data during the 1978-1982 period and the last half of 1985 if some stratospheric contribution were added to the PNL data. The PNL data set includes the El Chichon aerosol in the extra kilometer of the stratosphere and includes any aerosol in the troposphere not yet scavenged. The combined contributions may explain why the PNL data are generally higher during the El Chichon disturbance.

In Figure 8, three smoothed data sets are plotted: the SAM II (73°N), the PNL mid-latitude data (46.4°N), and the Mauna Loa data (19.5°N).

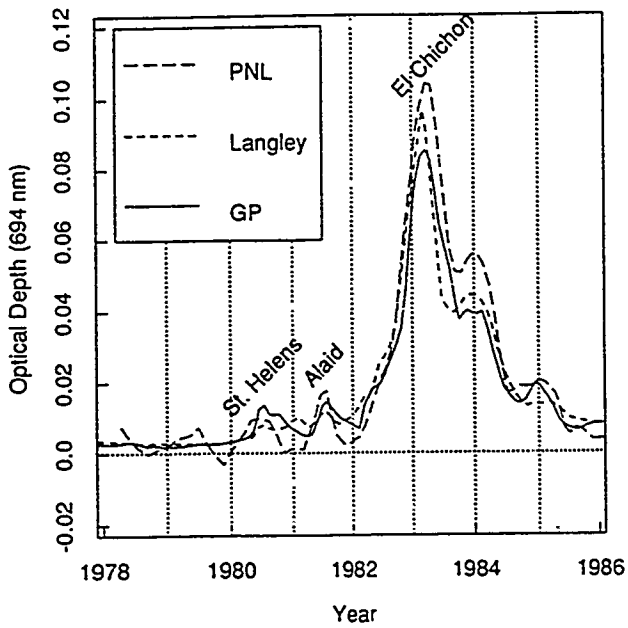

Fig. 6. Time series comparison of three distinct mid-latitude data sets of volcanic aerosol optical depth normalized to 694.3 nm.

The polar data are reasonably well correlated with the mid-latitude data, but have a lower amplitude. The St. Helens, Alaid, and El Chichon peak values are about one-half the mid-latitude optical depth. One notable difference is the absence of winter peaks during the decay of the El Chichon volcanic perturbation. McCormick et al. [1984] and Hofmann and Rosen [1987] suggested that a possible cause of the winter peaking at mid-latitudes was equatorward transport of stratospheric mass from the polar regions. There is no obvious hint in the polar data of any deviation from an exponential decrease. However, if we increase the time resolution of the north polar data, which is possible given the excellent coverage by SAM II, we see evidence in Figure 9 of transport both into and out of the region during the winters of 1983 and 1984. The 694.3-nm lidar data at Mauna Loa are presented for the period after the peak El Chichon loading. Measurements indicate optical depths in excess of 0.3 for observations made soon after the eruption [DeLuisi et al., 1983]. We have not plotted these data, since our main concern here is the decay period. An examination of the Mauna Loa curve suggests a repeating pattern. An exponential decay throughout most of the year in 1983 and 1984 is accelerated during the winter. The

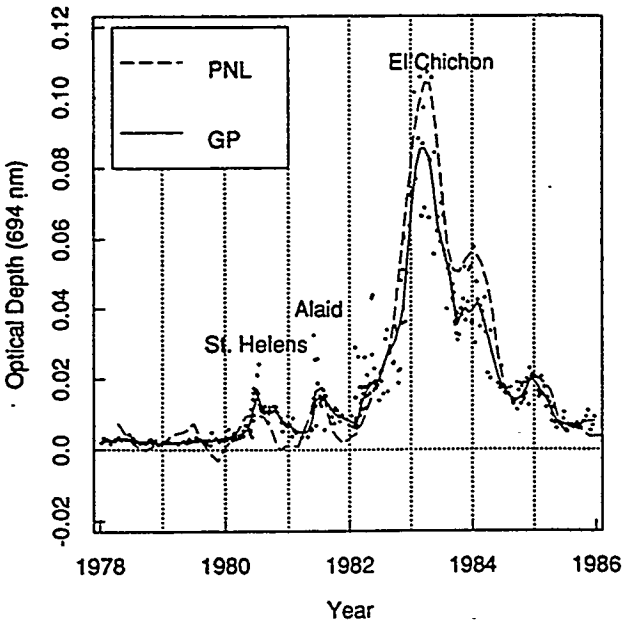

Fig. 7. Time series comparison of PNL and GP volcanic aerosol optical depths at 694.3 nm. The GP (47.5°N) data set is plotted, along with a smoothed fit to the data (solid line). The dashed line is the smoothed PNL (46.4°N) data interpolated to 694.3 nm.

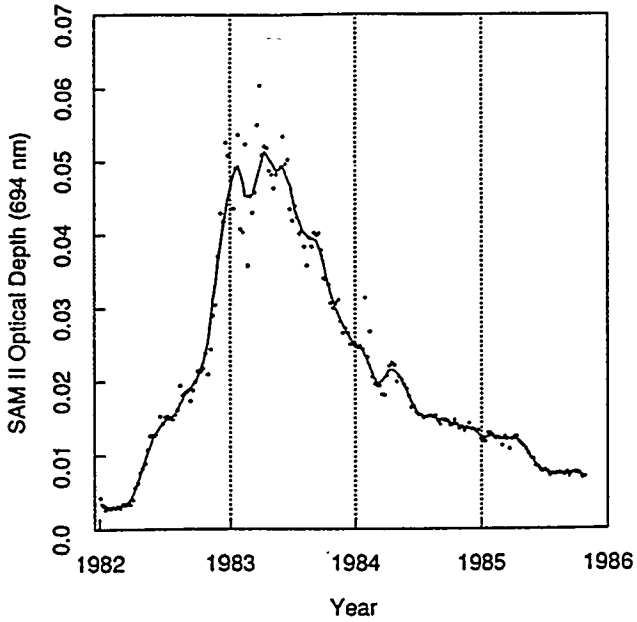

Fig. 9. Time series plot and estimate of SAM II volcanic optical depths at 694.3 nm. The time resolution of the estimate is higher here than in Figure 8, revealing more structure in the winter maxima.

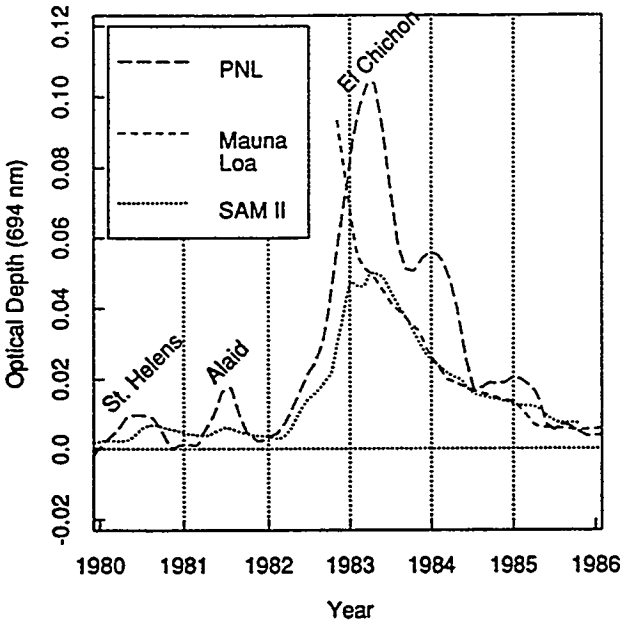

Fig. 8. Time series comparison of PNL (46.4°N), Mauna Loa (19.5°N), and SAM II (73°N) volcanic optical depths at 694.3 nm.

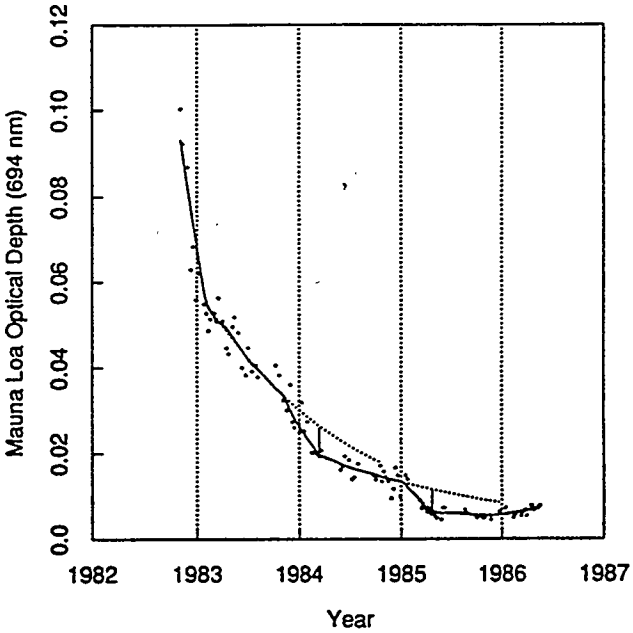

Fig. 10. The Mauna Loa data of Figure 8 expanded to define winter dips. The dotted lines are exponential fits to pre-winter data and extrapolations to expected values assuming no dips. Vertical solid lines are estimates of dip depths.

an extrapolation of the exponentials is about 0.007 optical depths in 1984 and 0.005 in 1985 as shown in Figure 10. This optical depth decrease is consistent with the observed perturbation magnitudes at mid-latitudes. This seasonal transport would appear to be the most significant contributor to the secondary maxima at mid-latitudes in the fall and winter after the 1983 El Chichon magnitude of the decrease over that expected from peak with some contribution from the polar regions as noted above. Dyer and Hicks [1968] were the first to consider this as part of a plausible explanation for the secondary maxima. We believe that this explanation is consistent with the available data and may be sufficient to explain the winter increases.

5. Discussion

To have the greatest accuracy, ground-based radiometer measurements should be made at every opportunity when the path to the sun is clear to gather as complete a record as possible; they should include a period of known minimal stratospheric loading to understand the seasonality of the tropospheric variations; and they should have sufficient spectral resolution to calculate the size of the intruding aerosol. Two pyrheliometric studies, which included background measurements before the 1980s, detected the impact of El Chichon [Rao and Bradley, 1983; Wendler and Kodama, 1986], but the broadband measurements allowed no inference of size. Spectral sunradiometer measurements were obtained by Davies et al. [1988] and Levizzani and Prodi [1988]. These studies could yield unambiguous information about the El Chichon aerosol wavelength dependence, but a clean measurement of seasonal aerosol variation before the eruption was not obtained. However, if the stratosphere remains unperturbed for the next year or so, the background variation could be determined using post-eruption data.

The advantages of ground-based sunradiometry over other techniques for measuring the volcanic impacts include cost, frequency, spectral resolution, and, perhaps, a truer measure of total volcanic aerosol impact. The cost advantages of a passive, ground-based measurement over an airborne or active system are obvious. If the surface system is automated and reliable, it reduces maintenance costs and allows measurements at every clear-sun opportunity. Whereas airborne measurements are made infrequently because of cost and complexity, surface measurements can be made during any cloud-free period. Sunphotometers typically measure at several wavelengths, providing an opportunity to obtain size information not available with some other techniques, for example, lidars. Ground-based radiometry measures actual aerosol perturbations by differencing. Once a background is established for a quiescent stratosphere, the perturbation measured is that to the total atmosphere. While most of the perturbation is in the stratosphere, some upper tropospheric volcanic aerosol may linger before scavenging, and it is included in the measurement performed by differential sunradiometry.

The disadvantages of this technique are limited time and height resolution. Since the troposphere is extremely variable, time averaging is required to extract meaningful results. One possible solution to this is to sample from a high mountain peak. If the tropospheric load is low and variability is small, then higher time resolution may be possible. Mauna Loa would be a prime site. Sun radiometry cannot readily provide height resolution, although by making use of high air mass data it may be possible to mathematically invert to obtain some height discrimination. Absolute accuracy with the differential technique is 0.01 optical depths, at a minimum, as explained in section 2 and Appendix B. This is a lower sensitivity than lidar measurements, for example, but sufficient if one is primarily interested in significant climatic events.

In section 4 the GP lidar data and the PNL sunradiometry data compared favorably. Several coincident measurements were made with airborne sunradiometers nearer to the PNL site in longitude than GP and near the same latitude. The point measurements of Shah and Evans [1984], Spinhirne [1983], Dutton and DeLuisi [1987], Swissler et al. [1983], and Spinhirne and King [1985] are roughly 20% higher than the PNL data. The agreement, however, may be considered good since all measurements were made within four months of the peak, and the smoothing procedure can underestimate peak values.

The assumption during the planning for this study was that the El Chichon aerosol would serve as a tracer to increase our understanding of transport processes in the lower stratosphere. Figure 9 and the discussion in section 4 suggests that there is some evidence for an equatorward transport from the polar regions. There is fair evidence in Figures 8 and 10 that the obvious transport from low latitudes to mid and high latitudes that occurred during the fall of 1982 [Hofmann, 1987], is repeated on a smaller scale the following two winters. Jager and Carnuth [1987] suggested that the winter maxima are simply the result of a lower tropopause, that is, a thicker stratosphere, during the winter. To increase the total aerosol, however, there must be transport into the region, and it is probable that a major contributor is aerosol from reservoirs at both high and low latitudes.

After this paper was submitted, an earlier study of the Agung eruption by Dyer and Hicks [1968] was brought to our attention. They used broadband solar beam attenuation before and after Agung's eruption to follow volcanic aerosol decay in both hemispheres. Their southern hemisphere data for this southern hemisphere volcano are remarkably similar to our results with exponential decay interrupted by winter maxima at mid and polar latitude sites.

Appendix A

Measurements and Analysis

Table A1 contains quarter-year estimates of the volcanic aerosol optical depth obtained from ground-based sunradiometry. The central wavelengths and the full widths at half maximum of the filters used are 429-2, 486-2, 535-3, 785-20, and 1010-30 nm. The estimates are for the period between 1979.5 and 1987.5. Data outside this range are not reported because the estimating procedure can produce unphysical results at the terminating points of the time series. Bear in mind that the error in estimating aerosol optical depth is on the order of 0.01 implying that many of the smaller entries are not statistically significant. The estimating process is described here.

The measurements are made using a computer-controlled, sun-tracking telescope that senses direct solar radiation every five minutes from sunrise to sunset (Kleckner et al. [1981] give a full description of the instrument). A total column optical depth is calculated using the Langley technique (Michalsky and Stokes [1983] provide a full explanation of the procedure), which assumes an exponential decrease in radiation with increasing air mass and stable conditions during the measurement period. This optical depth requires a straightforward correction for molecular scattering and a correction for molecular absorption. In practice, molecular absorption features other than the broad ozone Chappuis band are avoided, and corrections for ozone are applied using mean seasonal values for the latitude and longitude [Van Heuklon, 1979]. The result is a total column extinction resulting solely from the absorption and scattering by atmospheric aerosol.

As stated in section 2, the smoothing procedure [Cleveland, 1979] was selected as the method to estimate the mean seasonal behavior of the background aerosol. Several studies indicate that 1978 and 1979 were years when the strato-

TABLE A1. Volcanic Aerosol Optical Depth Estimates

Time	428	486	535	785	1010
1979.50	0.004	0.007	0.005	0.007	0.007
1979.75	0.001	0.003	0.001	0.000	0.000
1980.00	0.005	0.004	-0.002	0.000	0.000
1980.25	0.020	0.013	0.008	0.007	0.004
1980.50	0.020	0.020	0.016	0.010	0.007
1980.75	0.007	0.007	0.008	0.005	0.004
1981.00	0.009	0.007	0.007	0.001	0.001
1981.25	0.022	0.017	0.015	0.005	0.003
1981.50	0.047	0.042	0.035	0.017	0.012
1981.75	0.016	0.019	0.013	0.005	0.003
1982.00	0.020	0.019	0.015	0.003	0.002
1982.25	0.041	0.032	0.027	0.010	0.005
1982.50	0.062	0.052	0.043	0.021	0.013
1982.75	0.076	0.069	0.060	0.040	0.029
1983.00	0.105	0.096	0.093	0.080	0.066
1983.25	0.122	0.107	0.107	0.102	0.091
1983.50	0.067	0.064	0.066	0.072	0.071
1983.75	0.062	0.054	0.053	0.050	0.048
1984.00	0.066	0.057	0.057	0.055	0.045
1984.25	0.057	0.044	0.045	0.045	0.035
1984.50	0.020	0.016	0.017	0.018	0.015
1984.75	0.036	0.025	0.023	0.019	0.015
1985.00	0.033	0.024	0.023	0.020	0.016
1985.25	0.029	0.019	0.018	0.017	0.016
1985.50	0.005	0.003	0.001	0.005	0.007
1985.75	0.012	0.007	0.006	0.006	0.005
1986.00	0.006	0.001	0.001	0.004	0.003
1986.25	0.008	0.001	0.002	0.005	0.004
1986.50	0.020	0.013	0.011	0.010	0.008
1986.75	0.020	0.017	0.016	0.013	0.008
1987.00	0.011	0.008	0.008	0.006	0.004
1987.25	0.015	0.009	0.009	0.006	0.005
1987.50	0.005	0.004	0.002	0.001	0.001

sphere was extremely clean [Hofmann and Rosen, 1987; McCormick et al., 1984; Jager, 1987a]. The background included April 1978 to April 1981, and July 1987 to May 1988, inclusively. (Note that the year in which St. Helens erupted was included to increase the background coverage in some months, since it showed little enhancement relative to the earlier years.) An estimate of volcanically unperturbed seasonal behavior was then obtained from an amended data set in which the last half year was prepended, and the first half year was appended. This was necessary to preclude unphysical swings at the boundaries. Figure A1 is an example of this background estimation procedure for the aerosol optical depth data at 785 nm. The maximum occurs in mid-spring at this site and the minimum in late fall. The secondary peak in the mid-summer is repeated in several of the background years and is therefore real. To estimate the volcanic perturbation, a background estimate appropriate for the time of year is subtracted from each point in the data set. An estimate is then made using these points that represents our estimate of the time dependent volcanic perturbation.

Appendix B

Uncertainty and Validation

Measurement of the stratospheric aerosol burden from ground-based radiometry is confounded by interference from a noisy tropospheric aerosol component. Consequently, we have had to employ

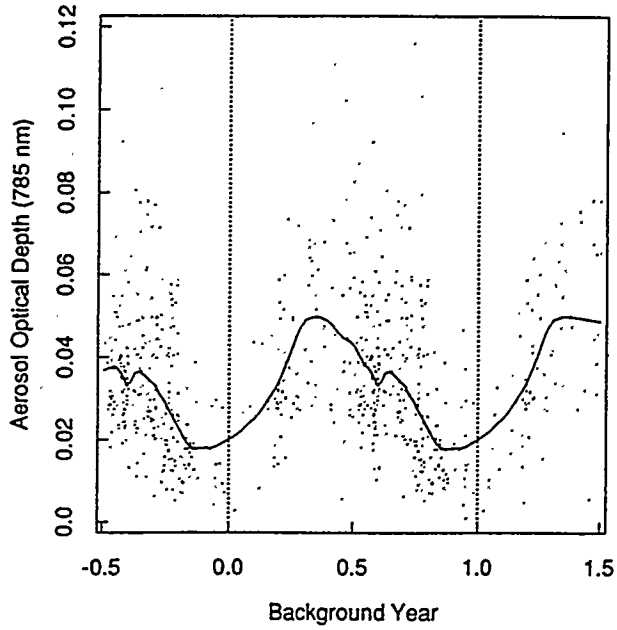

Fig. A1. Smoothed estimate of the seasonal dependence of the background optical depth at 785 nm. Last half-year data are prepended and first half appended to avoid unphysical behavior at the beginning and end of the year.

the rather complicated and certainly non-standard analysis technique described in section 2 to extract the volcanic signal from the measurements. It is evident at a glance that our technique permits qualitative detection of large stratospheric perturbations from the ground-based data. It is not immediately clear how to assess the quantitative accuracy of the estimates of stratospheric aerosol optical depth, however.

We have adopted three approaches for validating our technique and obtaining quantitative uncertainty measurements. First, we have carried out a number of simulations, in which artificial data sets intended to mimic our optical depth data are generated, and then reduced using the same procedure we apply to the radiometric data. Second, we obtain point estimates of the variance associated with our stratospheric optical depths through use of the jacknife technique [Efron, 1982]. In this approach a fraction of the data, selected at random, is eliminated and the remaining data set reduced. Repetition of this process provides a set of values, from which standard statistical measures of uncertainty can be calculated. Finally, we compare our results with those obtained by several other investigators. This appendix discusses the first two of these tests, concluding with comments on additional sources of uncertainty that may not be adequately treated in the simulation experiments. Comparison with additional data sets is treated in section 4.

Simulation Experiments

Our technique for estimation of the stratospheric aerosol burden is based on the assumptions that there has been no significant trend in tropospheric aerosol burden at our observation site over the last decade, and that the annual cycle in tropospheric loading is reasonably regular. Given these assumptions, it is possible to test our data analysis procedures by Monte Carlo

simulation. In addition, such simulations provide insight into the power and limitations of ground-based radiometric instruments as monitoring devices for stratospheric aerosol.

The main features of our optical depth data sets are that they measure combined noisy tropospheric and (presumably) more regular stratospheric contributions, and that they are irregularly sampled, with a relatively high frequency of observation during summer months and a low frequency during winter months. We generate artificial data sets that have the same general characteristics as follows. Total aerosol optical depth is given as the sum of a tropospheric component and a stratospheric component

$$t_{aer} = t_{trop} + t_{strat}$$

The tropospheric component is assumed to vary sinusoidally in the mean over the year, with a maximum in summer and a minimum in winter

$$\langle t_{trop} \rangle = a + b \sin(3\pi/2 + 2\pi d/365) \qquad \text{(A1)}$$

where $\langle t_{trop} \rangle$ is the mean value of aerosol optical depth at a particular time of year, a is the annual mean, b is the amplitude of the annual oscillation, and d is the day of year. A time series of daily tropospheric optical depth values is randomly generated from a lognormal distribution, with the mean given by (A1), and constant standard deviation derived from the statistics of the observational data set. To this time series a stratospheric perturbation is added, having the form

$$\begin{aligned} t_{strat} &= 0 & d < d_0 \\ &= t_{max}\,(d-d_0)/(d_p-d_0) & d_0 < d < d_p \\ &= t_{max}\exp(-(d-d_p)/t) & d > d_p \end{aligned}$$

Here d_0 is the day at which the stratospheric perturbation begins, d_p the date of the peak, and t the time for its exponential decay to 1/eth of its peak value. In our experiments we have assumed linear growth over a 100-day period, and set t=200 days. We have carried out experiments at several values of t_{max}, the maximum perturbation.

After having generated a composite daily optical depth time series by adding the background and stratospheric components, we complete construction of the simulation data set by sampling with a frequency similar to that achieved in actual data collection. For a given day the probability of achieving a successful measurement ranges from 0.8 (summer) to 0.2 (winter). Because the scatter in the background data is large compared with observational uncertainties, we do not add any additional experimental noise.

We have carried out several simulations for each of the t_{max} values 0.02, 0.04, 0.06, 0.08, and 0.1 optical depths. The characteristics of the tropospheric aerosol used in the simulations (mean value, amplitude of the annual cycle, and standard deviation used in the lognormal distribution) were roughly average for the five wavelengths at which we have observations, and the qualitative results of the simulations were not sensitive to specific choice of parameters. Results for two simulation runs at t_{max} = 0.1 are shown in Figure A2; other results are similar. On balance, the simulations suggest that, given our assumptions regarding the background aerosol variability, our data collection and analysis

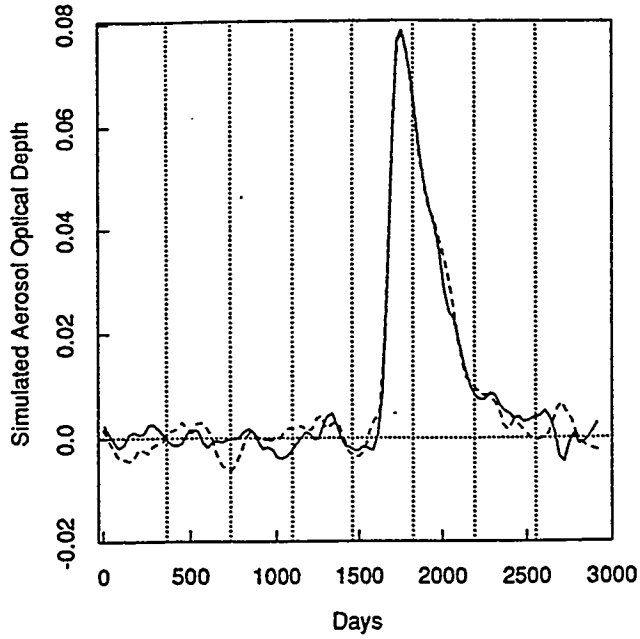

Fig. A2. The extracted perturbation curves using the procedures of section 2 on two simulations of aerosol data consisting of a sinusoidal background with lognormal noise and a superimposed peak perturbation of 0.1 optical depth.

procedures permit observation of extended perturbations (greater than or equal to one month in duration) of magnitudes less than or equal to 0.01 optical depths, and that greater sensitivity is probably practical. The major systematic error is an underestimate of the magnitude of sharp peaks; in the simulations typical peak values are about 85% of t_{max}. This tendency to underestimate peaks is not surprising, given the smoothing that is part of the analysis procedure, and is more pronounced for larger values of t_{max}. The simulations also show that random excursions in the estimate for t_{strat} comparable in magnitude to the oscillations in the observed decay of the El Chichon aerosol optical depths are rare, although not impossible.

In summary, these simulations roughly mimic the key features of our observational program. Our conclusion is that, from the simulated data, it is clearly possible to recover perturbations of as much as an order of magnitude less than that occasioned by El Chichon, and that, with some care, it may be possible to do even better. We add that it is certainly possible to generate more realistic simulations, incorporating such features as day-to-day correlations in background optical depth and probability of sampling, along with observational errors. The additional effort would be useful in a detailed assessment of the limitations of ground-based radiometric observations for routine stratospheric monitoring, but is not required to establish the reliability of the current results.

Determination of Confidence Intervals

We have employed the so-called jacknife technique [Efron, 1982] to obtain 90% confidence bands for our estimates of the stratospheric aerosol burden. The basic idea of this technique is to partition the complete data set into some

number N of disjoint groups of equal size, and to apply our analysis technique in turn to data sets obtained by deleting these groups from the full data set [Mosteller and Tukey, 1977]. From the resulting N curves, the variance of the calculated stratospheric enhancement can be estimated at any time point. In turn these estimates of variance can be used to establish confidence intervals.

More particularly, we have proceeded by partitioning the optical depth data set at each wavelength into 11 groups of roughly equal size, with individual data points assigned to the groups at random. We then execute our entire analysis procedure (including background determination) to compute 11 estimates of the El Chichon stratospheric perturbation, each based on the full data set less one of the groups. Figure A3 shows the envelope of these curves at 785 nm.

Based on these 11 curves, which we denote ti_{strat}, we construct "pseudocurves", Li_{strat}, from the equation

$$Li_{strat} = Nt_{strat} - (N-1)ti_{strat}$$

where t_{strat} is the estimated stratospheric burden obtained from applying the analysis to the full data set. The Li_{strat} correspond to what are called pseudovalues when the jacknife technique is applied to statistical procedures resulting in the generation of single quantities. Roughly speaking, Li_{strat} can be thought of as an influence function for the ith subset of the data.

In the jacknife technique, variance estimates are obtained simply from the variance of the pseudovalues. Figure 2 shows 90% confidence intervals computed in this fashion at 785 nm; the others are similar. In general, the confidence intervals are broadest at the short wavelengths, reflecting the fact that the tropospheric aerosol is more variable at those wavelengths. However, the confidence intervals are uniformly narrower than 0.01 optical depths at their broadest, and, at most times, are substantially narrower.

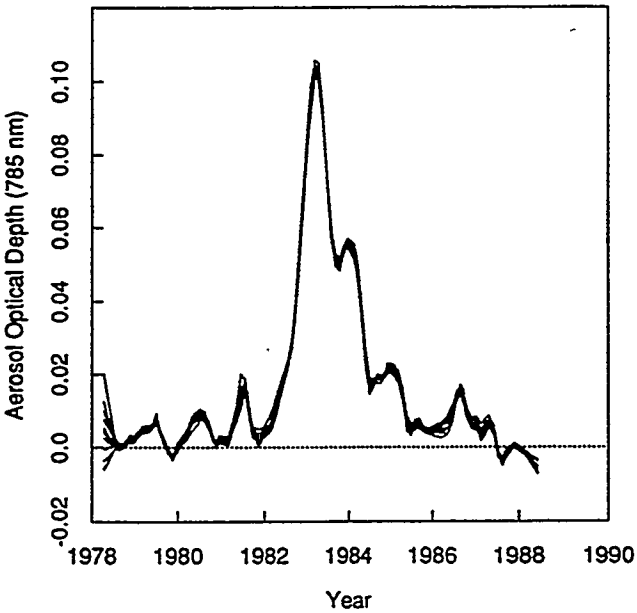

Fig. A3. Aerosol optical depth perturbation estimates for 785 nm with a random selection of one-eleventh of the data removed before the estimate is made.

This jacknife analysis demonstrates that the scatter caused by the high variability of the tropospheric aerosol does not prevent a stable and reliable estimate of the stratospheric perturbation. The variance in the estimates varies by as much as an order of magnitude as a function of time. Interestingly, the variance appears to be lowest in the winter months, when the density of data collection is lowest (and therefore the time window over which the data is smoothed is broadest), with most of the peaks occurring in the summer months.

As a final note, it is important to remember that these confidence intervals are not confidence intervals for the actual stratospheric enhancement in aerosol optical depth. Rather, they are confidence intervals for our measure of that perturbation, and, consequently, apply to a smoothed stratospheric optical depth. Further, these intervals account only for the influence of variability in the data, and have not been adjusted to take into account systematic errors, such as a failure in one of our basic assumptions.

Additional Considerations

Tests of internal variability in the data and the reliability of our analysis procedures have been described in the preceding paragraphs. It is also necessary to address uncertainty introduced by the possibility of errors in our underlying assumptions. The most important of these assumptions are, first, that there is no underlying secular trend in the optical depth as a result of tropospheric aerosol, and, second, that the year-to-year variability of the tropospheric aerosol is small compared with the stratospheric loading under study. Failures of either of these assumptions could severely affect the reliability of our results.

There appears to be no indication in our data of either a long-term trend in t_{trop} or of substantial excursions affecting single years. (Of course, there are numerous short-term excursions; the analysis technique is explicitly designed to minimize their influence.) Two factors to note are, first, the apparent return to background levels in 1987 of our data at all wavelengths, and, second, the limited magnitude of fluctuations in the pre-El Chichon period. In addition, a much longer time series of optical depth data taken at a different location [Szymber and Sellers, 1985] shows no trend in optical depth over a thirty-year period partially overlapping our data collection interval. Consequently, we believe that our assumptions are reasonably accurate.

Conclusion

We believe that the estimates of the stratospheric optical depth shown in Figure 3 and reported in Table A1 are reliable to within the confidence intervals shown, although sharp features are blurred by the smoothing characteristics of our analysis technique. Monte Carlo simulation experiments indicate that our current data collection and analysis protocols permit detection of stratospheric events at least an order of magnitude smaller than El Chichon, and it is quite possible that refinement of the approach could permit even better performance. There does not appear to be any evidence confounding our key underlying assumptions regarding the stability of the tropospheric aerosol burden at our measurement site. Comparisons with data of other inves-

tigators, discussed in section 4, further substantiate these conclusions.

Acknowledgments. The authors would like to thank J. DeLuisi, H. Jager, and P. McCormick for providing their numerical data used in the intercomparisons. M. King kindly provided the code for inverting the aerosol optical depth to get size distribution. The referees' comments helped clarify our presentation and revealed a similar study of Agung in the southern hemisphere. This work was partially supported by the U.S. Department of Energy, Office of Basic Energy Sciences, under contract DE-AC06-76RLO 1830.

References

Brogniez, C. and J. Lenoble, Modeling of the stratospheric aerosols from zonally averaged SAGE profiles, J. Geophys. Res., 92, 3051-3060, 1987.

Cleveland, W.S., Robust locally-weighted regression and smoothing scatterplots, J. Am. Stat. Assoc., 74, 829-836, 1979.

Davies, J.A., R. Schroeder, and L.J.B. McArthur, Surface-based observations of volcanic aerosol effects, Tellus, 40B, 154-160, 1988.

DeLuisi, J.J., E.G. Dutton, K.L. Coulson, T.E. DeFoor, and B.G. Mendonca, On some radiative features of the El Chichon volcanic stratospheric dust cloud and a cloud of unknown origin observed at Mauna Loa, J. Geophys. Res., 88, 6769-6772, 1983.

DeLuisi, J., T. DeFoor, K. Coulson, and F. Fernald, Lidar observations of stratospheric aerosol over Mauna Loa Observatory: 1982-1983, Data Rep. ERL ARL-5, NOAA Silver Springs, Md., Feb. 1985.

DeLuisi, J., T. DeFoor, and D. Longenecker, Lidar observations of stratospheric aerosol over Mauna Loa Observatory: 1984-1985, Data Rep. ERL ARL-9, NOAA Silver Springs, Md., Sept. 1986.

DeLuisi, J.J., D.U. Longenecker, C.L. Mateer, and D.J. Wuebbles, An analysis of northern midlatitude Umkehr measurements corrected for stratospheric aerosols for 1976-1986, J. Geophys. Res., 94, 9837-9846, 1989.

Dutton, E. G. and J. J. DeLuisi, Aerosol optical depth and ratios of diffuse-sky to total solar irradiance measured from aircraft following the eruption of El Chichon, Data Rep. ERL ARL-12, NOAA Silver Springs, Md., June 1987.

Dyer, A.J. and B.B. Hicks , Global spread of volcanic dust from the Bali eruption of 1963, Q. J. R. Meteorol. Soc., 94, 545-554, 1968.

Efron, Bradley, The Jacknife, the Bootstrap, and Other Resampling Plans, 92 pp., Society for Industrial and Applied Mathematics, Philadelphia, Pa., 1982.

Hirono, M. and T. Shibata, Enormous increase of stratospheric aerosols over Fukuoka due to the volcanic eruption of El Chichon in 1982, Geophys. Res. Lett., 10, 152-154, 1983.

Hofmann, D.J., Perturbations to the global atmosphere associated with the El Chichon volcanic eruption of 1982, Rev. Geophys., 25, 743-759, 1987.

Hofmann, D.J. and J.M. Rosen, On the background stratospheric aerosol layer, J. Atmos. Sci., 38, 168-181, 1981.

Hofmann, D.J. and J.M. Rosen, On the temporal variation of stratospheric aerosol size and mass during the first 18 months following the 1982 eruptions of El Chichon, J. Geophys. Res., 89, 4883-4890, 1984.

Hofmann, D.J. and J.M. Rosen, On the prolonged lifetime of the El Chichon sulfuric acid aerosol cloud, J. Geophys. Res., 92, 9825-9830, 1987.

Jager, H., The stratospheric aerosol layer observed by lidar over Garmisch-Partenkirchen, 1976-1981, data report, IFU Rep. 87010, Fraunhofer-Inst. for Atmos. Environ. Res., Garmisch-Partenkirchen, Federal Republic of Germany, 1987a.

Jager, H., The stratospheric aerosol layer observed by lidar over Garmisch-Partenkirchen, 1982-1985, data report, IFU Rep. 87012, Fraunhofer-Inst. for Atmos. Environ. Res., Garmisch-Partenkirchen, Federal Republic of Germany, 1987b.

Jager, H. and W. Carnuth, The decay of the El Chichon stratospheric perturbation, observed by lidar at northern midlatitudes, Geophys. Res. Lett., 14, 696-699, 1987.

Junge, C.E., Air Chemistry and Radioactivity, 382 pp., Academic, San Diego, Calif., 1963.

King, M.D., D.M. Byrne, B.M. Herman, and J.A. Reagan, Aerosol size distributions obtained by inversion of spectral optical depth measurements, J. Atmos. Sci., 35, 2153-2167, 1978.

King, M.D., Harshvardan, and A. Arking, A model of the radiative properties of the El Chichon stratospheric aerosol layer, J. Clim. Appl. Meteorol., 23, 1121-1137, 1984.

Kleckner, E.W., J.J. Michalsky, L.L. Smith, J.R. Schmelzer, R.H. Severtsen, and J.L. Berndt, A multipurpose computer-controlled scanning photometer, Rep. PNL-4081, Pac. Northwest Lab., Richland, Wash., 1981.

Levizzani, V. and F. Prodi, Atmospheric effects of the El Chichon volcanic eruption observed by a multiwavelength sun-photometer, 1982-1985, J. Geophys. Res., 93, 5277-5286, 1988.

Mauldin, L.E., III, N.H. Zaun, M.P. McCormick, J.H. Guy, and W.R. Vaughn, Stratospheric aerosol and gas experiment II instrument: A functional description, Opt. Eng., 24, 307-312, 1985.

McCormick, M.P. and C.R. Trepte, Polar stratospheric optical depth observed between 1978 and 1985, J. Geophys. Res., 92, 4297-4306, 1987.

McCormick, M.P., T.J. Swissler, W.H. Fuller, W.H. Hunt, and M.T. Osborn, Airborne and ground-based lidar measurements of the El Chichon stratospheric aerosol from 90 deg N to 56 deg S, Geofiso. Int., 23, 187-221, 1984.

Michalsky, J.J. and G.M. Stokes, Mt. St. Helens' aerosols: Some tropospheric and stratospheric effects, J. Clim. Appl. Meteorol., 22, 640-648, 1983.

Mosteller, F. and J.W. Tukey, Data Analysis and Regression, a Second Course in Statistics, 588 pp., Addison-Wesley, Reading, Mass., 1977.

Pearson, E.W., B.A. LeBaron, and J.J. Michalsky, Decay of the El Chichon perturbation to the stratospheric aerosol layer: Multispectral ground-based radiometer observations, Geophys. Res. Lett., 15, 24-27, 1988.

Post, M.J., Lidar observations of the El Chichon cloud at 10.6 micrometers, Geophys. Res. Lett., 11, 846-849, 1984.

Rampino, M.R. and S. Self, The atmospheric effects of El Chichon, Sci. Am., 253, 48-57, 1984.

Rao, C.R.N. and W. A. Bradley, Effects of the El Chichon volcanic dust cloud on insolation measurements at Corvallis, Oregon (U.S.A.), Geophys. Res. Lett., 10, 389-391, 1983.

Shah, G.M. and W.F.J. Evans, Aircraft latitude

survey measurements of the El Chichon eruption cloud, Geophys. Res. Lett., 11, 1125-1128,1984.

Spinhirne, J.D., El Chichon eruption cloud: Latitudinal variation of the spectral optical thickness for October 1982, Geophys. Res. Lett., 10, 881-884, 1983.

Spinhirne, J. D. and M. D. King, Latitudinal variation of spectral optical thickness and columnar size distribution of the El Chichon stratospheric aerosol layer, J. Geophys. Res., 90, 10607-10619, 1985.

Swissler, T.J., M.P. McCormick, and J.D. Spinhirne, El Chichon eruption cloud: Comparison of lidar and optical thickness measurements for October 1982, Geophys. Res. Lett., 10, 885-888, 1983.

Szymber, R.J. and W.D. Sellers, Atmospheric turbidity at Tucson, Arizona, 1959-83: Variations and their causes, J. Clim. Appl. Meteorol., 24, 725-734, 1985.

Van Heuklon, T.K., Estimating atmospheric ozone for solar radiation models, Solar Energy, 22, 63-68, 1979.

Wendler, G. and Y. Kodama, Effect of the El Chichon volcanic cloud on the surface radiative regime in central Alaska, J. Clim. Appl. Meteorol., 25, 1687-1694, 1986.

Brock A. LeBaron and Erik W. Pearson, Battelle-Pacific Northwest Laboratories, P.O. Box 999, Richland, WA 99352.

Joseph J. Michalsky, Atmospheric Sciences Research Center, State University of New York at Albany, 100 Fuller Rd, Albany, NY 12205.

(Received May 12, 1989;
revised August 20, 1989;
accepted October 4, 1989.)

PNL-4081
UC-37

A MULTIPURPOSE COMPUTER-CONTROLLED SCANNING PHOTOMETER

E.W. Kleckner
J.J. Michalsky
L.L. Smith
J.R. Schmelzer
R.H. Severtsen
J.L. Berndt

November 1981

Prepared for U.S. Department of Energy
under Contract DE-AC06-76RLO 1830

Pacific Northwest Laboratory
Richland, Washington 99352

SUMMARY

The description of a mobile, multipurpose computer-controlled scanning photometer is presented. This report supersedes two earlier partial descriptions of the instrument (Kleckner, Smith and Hoch 1975; Kleckner, Michalsky and Smith 1978) and presents the instrument as it is presently configured.

The scanning, altazimuth instrument has a fairly narrow field of view (1.5° for daytime work and .5° for nighttime) and can point to any position within a sphere. Twelve interference filters provide the wavelength discrimination important in the aeronomical emission feature studies and the solar spectral distribution characterization program. The basic philosophy was to design the software programs to acquire a variety of solar and geophysical data which would be useful to a wide audience. The photometer design was such that most of the decision-making was incorporated in the software of the computer to allow needed or desired changes to be made readily.

ABSTRACT

This paper presents a design for a multipurpose computer-controlled scanning photometer capable of measuring optical radiation ranging in intensity from the subvisual light levels associated with night sky airglow emissions to the intense flux levels of direct sunlight. The instrument has twelve interference filters for wavelength selection, a 2.5° field of view for nighttime observations, and a 1.5° field of view for daytime observations. A photomultiplier tube is used as the low light-level detector, and a silicon-PIN photodiode serves as the insolation detector. A particular measurement sequence is programmed into the instrument and can be modified by reading a cassette tape in the field. Normal operation is fully automatic. Visits to change the data cassette tapes and to service the instrument are made every four days with extensive maintenance and calibration trips semi-annually. In addition to controlling the measurement sequence, the computer provides a means of compressing the data by a factor between two and three before recording it. The procedures used in calibrating these absolute measurements are detailed.

CONTENTS

INTRODUCTION 1
HARDWARE 2
Optical 2
Mechanical. 5
Electronic. 7
Environmental 13
CONTROL SYSTEM 15
OBSERVATIONS 17
Aeronomy. 17
Insolation. 21
Other Programs. 24
CALIBRATION. 24
Aeronomy. 25
Insolation. 27
NETWORK DESCRIPTION. 28
ACKNOWLEDGEMENTS 29
REFERENCES 30

I. INTRODUCTION

As originally conceived, the photometer described in this report was to answer a need in middle atmospheric studies for global measurements of visible emission features associated with the aurora and airglow. The desire was to eliminate the tedium of tending a photometer which repeated a sequence of all-sky scans from dusk to dawn. An improved mechanical design which avoided problems associated with cables wrapping about the rotation axis of the photometer was a further requirement.

The prototype unit was designed with an altazimuth system of mirrors that transferred parallel rays from a distant source to a conventional imaging optical train which remained stationary within the photometer. The mechanical design that allowed cableless operation of this system is described in Section II. The scan/filter sequence was wired onto the control board of the instrument. Scanning was initiated and concluded each night via a photometric threshold detector (cadmium sulfide photocell) mounted on the outside of the instrument. The photometer was housed in a fabricated aluminum cube approximately 0.76 meters on a side covered by a Plexiglas hemispherical dome with a diameter of 0.71 meters. With the exception of a few minor mechanical problems (e.g., screws loosening, air conditioners failing), the photometer functioned reliably in a harsh eastern Montana environment from September 1975 until March 1979 when it was replaced by the present-generation photometer.

Two circumstances led us to reconfigure the photometer. A major limitation of the first unit was its inflexibility, i.e., changing the observing routine entailed rewiring the control board within the instrument. Renewed interest in the use of the sun as an energy source led us to consider a redesign of the instrument to include daytime measurements. The second-generation photometer, which will be discussed in this paper, includes changes to accommodate both of these needs, as well as further updating.

In Section II, the hardware of the instrument is discussed, including the mechanical, optical, electronic, and environmental aspects of the instrument. In Section III, the control system for the instrument is described. In Section IV, typical observing routines for the night and day programs are discussed. Section V contains a description of the procedures used in calibrating the daytime and nighttime photometers. Finally, the instrument sites selected and rationale for their selection are presented in Section VI.

II. HARDWARE

This section describes the instrument hardware as it is presently configured. Parts and construction costs have remained relatively constant over the 4-5 years of the program due to experience gained in fabricating the units and the decreasing costs of electronic components. The photometer is, in essence, a computer-controlled altazimuth telescope with 13-cm optics. It is equipped for day and night operation with two, slightly different, sets of optics which image the objective on the two detectors used in the two programs.

A. Optical

A schematic representation of the optical train is given in figure 1. Parallel rays emitted from a distant source are transferred to the imaging optics via mirrors M1 and M2. A particular look direction is selected by positioning these two mirrors. Mirror M1 is rotated about a horizontal axis to choose a particular elevation angle, and mirrors M1 and M2 rotate together about a vertical axis to select a particular azimuth angle. The mirrors are elliptically-shaped flats with major and minor axes of 22.0 cm and 16.5 cm. They are front-surfaced with a protected silver coating which reflects over 98 percent of the light incident from 500 nm to well beyond both detector cutoffs in the near infrared (>1100 nm). Below 500 nm the reflectance is still quite high for all wavelengths covered by our filter set.

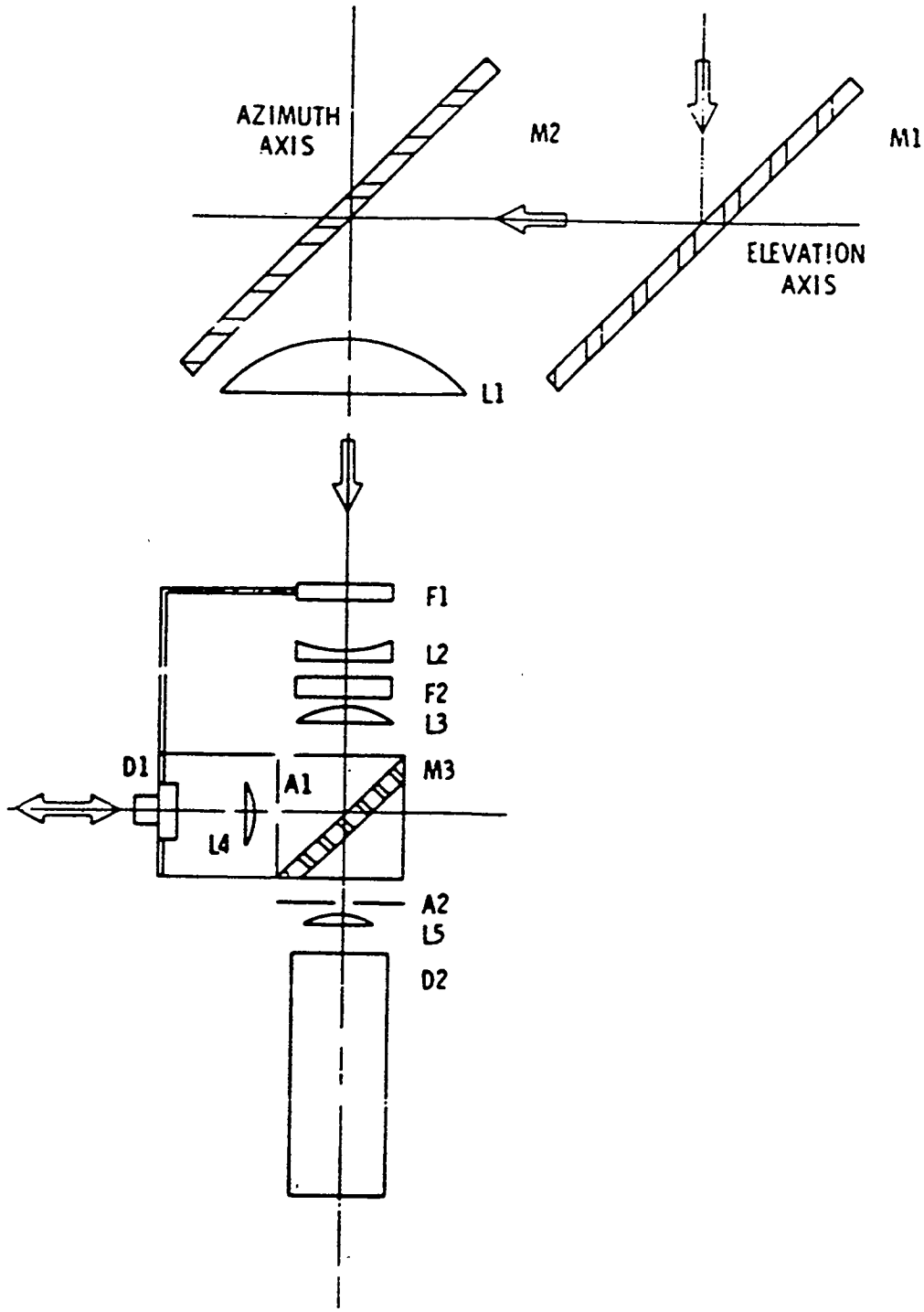

Figure 1. Schematic Diagram of the Optical Train of the Photometer.

Selection of the reflecting material was of some importance because of the polarizing properties of materials at oblique angles of incidence. Polarized radiation is not reflected equally at all angles of incidence (in our case this is not a problem since the angle of incidence is always 45°) or for all positions of the electric vector with respect to the plane defined by incident and reflected rays. This latter effect can produce a photometric signal that differs by greater than 20 percent for a highly polarized source (e.g., scattered sunlight) of constant intensity incident on an overcoated aluminum mirror. By matching the reflectances of the electric vector components parallel and perpendicular to the reflection plane, one can eliminate this problem. If a constant source is unpolarized (e.g., direct sunlight), there is no change (at the 1-percent level) in detected intensity for a light incident on aluminum or silvered mirrors.

After reflection from the two silvered mirrors, the optical path is conventional. L1 is a 12.7-cm diameter anti-reflection coated lens with a 20.3-cm focal length. Lens L2 has a 5.1-cm diameter and a focal length of -8.0 cm. It serves as a Ross zero corrector to render the rays through the interference filter, F2, nearly parallel. Lens L3 forms an image of the distant source at the 2.5° aperture A2 when assembly F1-M3 is out of the optical path, and when F1-M3 is in the optical path L3 forms a source image at the 1.5° aperture A1. L5 images the fixed virtual objective on the photocathode of the photomultiplier tube D2, and L4 images the virtual objective on the photodiode D1. These last two lenses minimize the effect of spatial inhomogeneities in the photomultiplier and photodiode responses by imaging a fixed optic on them. L1 has a large aperture to increase the throughput during nighttime observations. F1 of movable assembly F1-M3 is an iconal neutral density filter with a transmission of approximately 0.005 to attenuate direct solar radiation, and M3 is a silvered mirror that folds the optical path toward the solar detector.

B. Mechanical

The mechanical motions within the photometer are described here. This includes the scanning head, the filter wheel, and the motor-driven assembly F1-M3 (figure 1) which moves into and out of the optical path.

Figure 2 is a schematic representation of the altazimuth mount. A bi-directional stepping motor drives a dual shaft assembly which transmits power to either the upper ring gear 'A' or to both ring gears 'A' and 'B' according to the conditions of the magnetic brake and clutch. With the brake energized and the clutch free, ring gear 'A' is driven via the central shaft with ring gear 'B' clamped. This transmits power to worm gear 'C' effecting movement of mirror M1 about a horizontal axis thereby scanning in elevation angle. With the brake released and the clutch engaged, both shafts are driven simultaneously transmitting power to gears 'A' and 'B' such that the whole mount moves about a vertical axis, effecting azimuthal scanning. The azimuthal and elevation scan rates are 20° and 5° per second, respectively.

Coupled to each ring gear of the drive mechanism is an optical tachometer which produces a pulse output proportional to rotation. These pulses are sampled at a 400-Hz rate and allow determination of the angular displacement in azimuth and elevation. Since the tachometers are not absolute encoding devices, a zero position must be defined for each rotation axis. For the azimuth zero, the edge of a tab attached to the rotating upper head assembly is used to trigger an optical switch. A similar arrangement, attached to the elevation assembly, serves to define the elevation zero.

A 12-position filter wheel provides wavelength discrimination for both the daytime and nighttime programs. The 5.1-cm filters are spaced equally about the periphery of the 30.5-cm diameter wheel which is driven by a bi-directional stepping motor. Tabs are

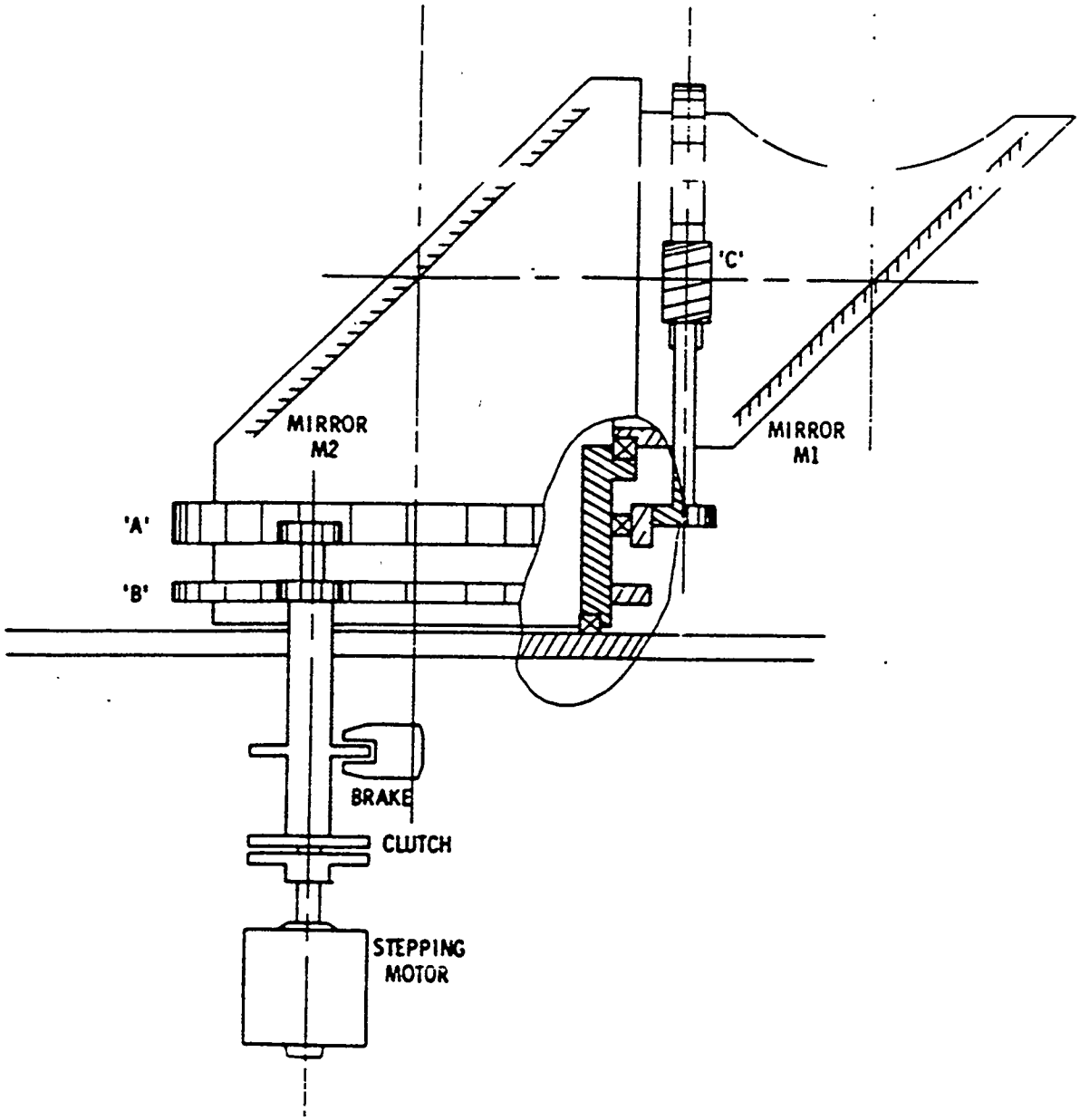

Figure 2. Schematic Diagram of the Altazimuth Drive System Showing the Principal Components.

mounted about the rim of the wheel in such a manner as to protrude and pass through a set of four equally-spaced optical switches which serve as "read" stations for filter positioning. Using "1" to indicate a tab-blocked optical switch and "0" to indicate no tab, the sequence 110111000100 is used to code filter position. The set of four optical switches interpreted as a decimal number then generates the numerical sequence (13, 11, 7, 14, 12, 8, 1, 2, 4, 9, 3, 6) as the 12-position filter wheel cycles through a revolution. A zero is generated by the "read" stations when the filters are not centered, e.g., during a filter change. The present set of filters used in all the instruments is given in Table 1. The first four are very narrow (1-2 nm FWHM) filters centered on auroral and airglow emission features and the fifth is a continuum filter for the nighttime observations. The next seven broad-band filters are selected to span the sensitivity of the photodiode used in the solar program. The narrow filters used at night are also used in some of the solar observations.

The assembly F1-M3 of figure 1 is a screw-driven carriage transported by a bi-directional motor. Positioning for day or night operation is defined by optical switches. In the day position, the optical path is through the neutral density filter F1 followed by a 90° reflection from the silvered mirror M3. At night, F1-M3 retracts. A photometric threshold detector mounted on the outside of the photometer governs the position assumed by the assembly.

C. Electronic

In the next few paragraphs, detectors used in the two photometers, signal acquisition, time-keeping, and recording are described. The minicomputer and its associated software that control these functions are discussed in Section III.

A significant problem with historical solar data is the accuracy with which much of it was taken. Detector stability

TABLE 1

Filter Wavelengths, Bandwidths, and Functions

Center λ(nm)	FWHM(nm)	Use
630.0	1	Night, Day
557.7	1	Night, Day
486.1	2	Night, Day
427.8	2	Night, Day
535.0	3	Night, Day
395.0	60	Day
470.0	100	Day
570.0	100	Day
680.0	120	Day
785.0	20	Day
900.0	160	Day
1010.0	30	Day

over long periods was difficult to maintain. In recent years photodiodes have proven quite suitable to this purpose. For this instrument a silicon PIN photodiode (EG&G HAV 4000) was chosen. The PIN diode has a number of characteristics which make it appropriate for this application: the response is linear to better than 1 percent over nine decades of incident light intensity; the response is constant to 0.5 percent over six months; it is physically rugged and will withstand well the effects of over-illumination. The photodiode is hermetically sealed in a package containing a high-gain FET input amplifier. Countering the positive aspects of the photodiode is the temperature dependence of the response, especially toward the long and short wavelength cutoffs. Figure 3 illustrates a typical response deviation as a function of temperature and wavelength for the type of photodiode used in the instrument (Application Note D3011C-1). By operating the diode in a zero-bias configuration, first-order variation of diode current with temperature is eliminated. To control the remaining variation shown in figure 3, the temperature is held at 20°±3°C to achieve an overall stability of better than 1 percent for all but the longest wavelength filter in Table 1. A fairly constant digitization of the intensity over the range of illumination that is typically encountered in the daytime operation can be maintained by selection of one of four gains. The gain, chosen under program control, is in increments of 32 for a range of 1:32,768.

For nighttime operation, the detector is a photomultiplier tube operated in the pulse-counting mode. The tube, an EMI 9558A, has an S-20 photocathode; consequently, it responds to wavelengths from 300-850 nm. A custom-designed magnetic lens was chosen to minimize the dark count resulting from the non-illuminated portion of the photocathode. The photomultiplier operates uncooled, but it is maintained at a fixed temperature of 20°±3°C. One would like to be able to detect reasonably bright auroral displays and barely detectable airglow phenomena with the same photomultiplier tube.

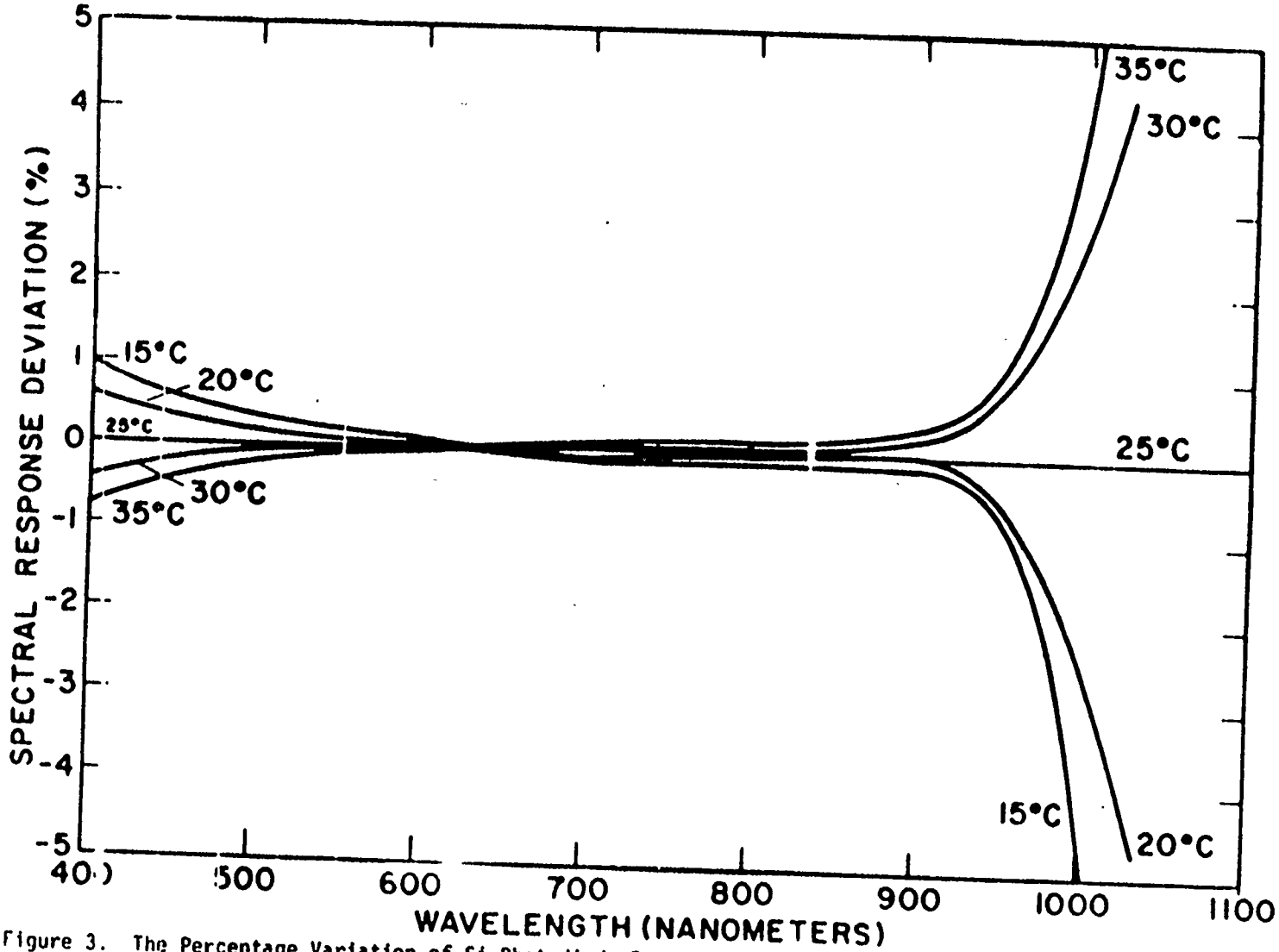

Figure 3. The Percentage Variation of Si Photodiode Response as a Function of Wavelength and Temperatur

To achieve this, the voltage at which the tube operates is chosen maximize the dynamic range. A conventional pulse amplifier-discriminator amplifies the photomultiplier tube output and prevents registration of pulses of low amplitude which result from electrons originating down the dynode chain from the photocathode.

Since the photometer is operated unattended, there is concern about protection of the photomultiplier tube from over-illumination by an intense aurora or, perhaps, a brilliant lightning display. For this purpose an electro-mechanical shutter which protects the photomultiplier tube is hard-wired to two protection devices. One is the photometric threshold sensor which sends a "close-shutter" signal if the sky becomes bright enough to turn it on. The other is an overcurrent circuit, built into the photomultiplier tube circuit, which also closes the shutter should the current from the tube exceed a predetermined value.

Data acquisition from the two detectors as well as other internal sources is schematically illustrated in figure 4. An analog multiplexer selects one of eight sources as input to a 10-V/100-kHz voltage-to-frequency converter. Low sampling rates with variable integration times and a maximum nonlinearity of the voltage-to-frequency converter of ±0.05 percent over 80 dB make this an ideal analog-to-digital conversion scheme consistent with our overall accuracy requirements. Besides the photodiode sensor, the other inputs to the analog multiplexer include, for test purposes, the photomultiplier high voltage, filter wheel temperature, outside temperature, a 5-Volt reference, a spare input, the output of a digital-to-analog converter used to check the self-consistency of the system and to provide an analog output for external monitoring devices, and a grounded input to check the stability of the electronics.

A digital multiplexer selects one of eight channels as input to a 16-bit counter. The counter is controlled by a variable time

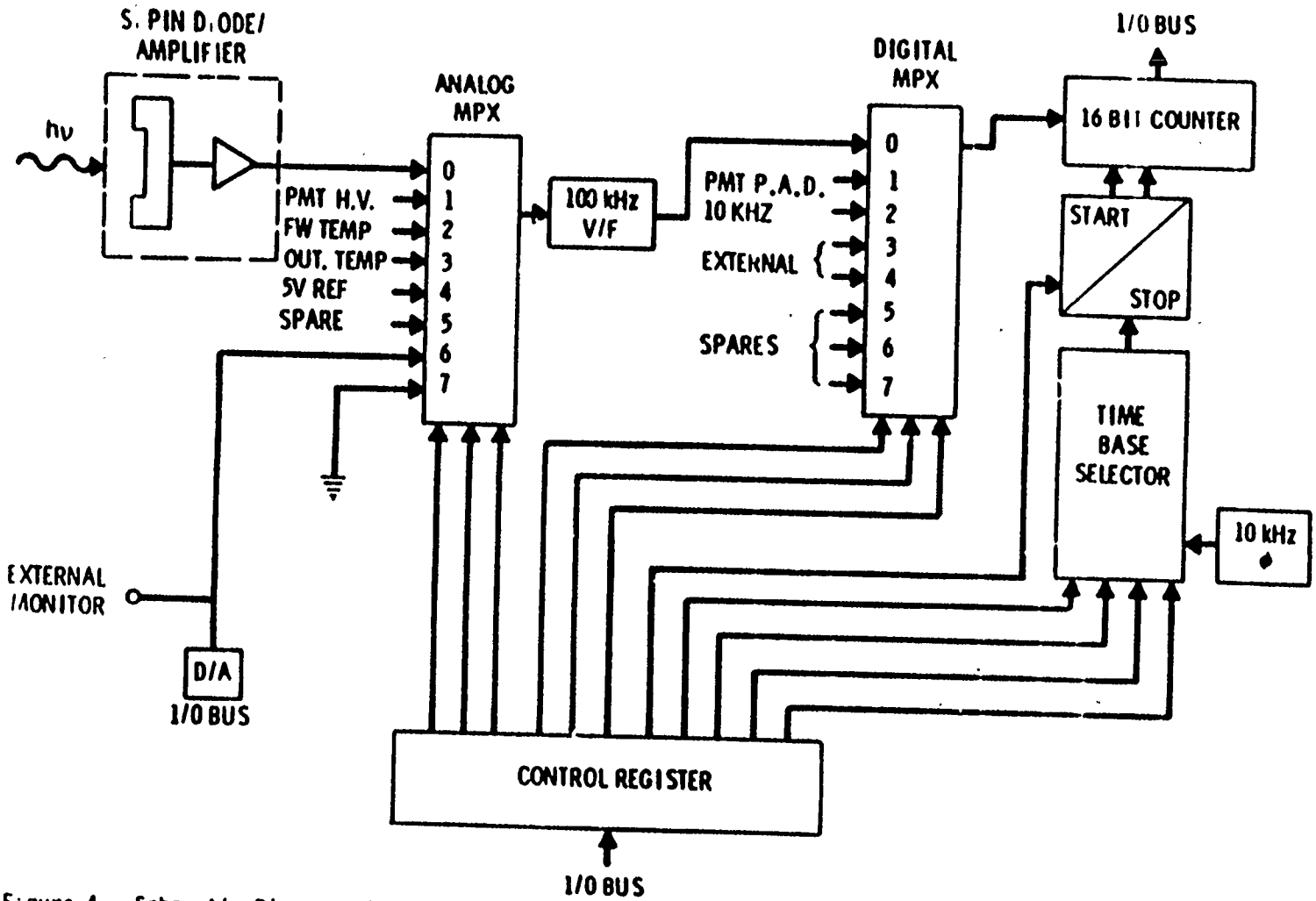

Figure 4. Schematic Diagram of the Data Acquisition System.

base which can assume one of 16 values. The minimum integration time is 100 .sec and the integration times increase by factors of two up to a maximum period of 3.2768 seconds. Besides the voltage-to-frequency converter, the digital multiplexer inputs include the photomultiplier tube output through the pulse amplifier-discriminator, a 10-kHz reference signal, two channels dedicated to external devices, and three spare inputs.

Instrument time is derived from the 60-kHz carrier signal broadcast by WWVB radio station of the National Bureau of Standards located at Fort Collins, Colorado. The time signal is received by an active antenna located near the instrument and the binary coded decimal signal is decoded by software to provide time of day in seconds from midnight (UT) and day of year. During times of poor reception, interpolation is provided by a crystal clock. Recording is on magnetic cassette tapes using a commercially available tape drive (Interdata or Sycor).

D. Environmental

Housing for the photometer was carefully considered because the photometers are operated at nearly constant interior temperatures. The narrow interference filters and photomultiplier tube used for the nighttime work and the photodiode sensor used during the day are all temperature-sensitive. Figure 5 is a photograph of the photometer exterior. The standard size pickup camper unit is well-sealed, with extra insulation built in. An electric baseboard heater together with an air-conditioning unit operate on a differential thermostat which maintains the temperature at 20°±3°C. A square plate 90 cm on a side and 2.5-cm thick carries the optical-mechanical assembly of the photometer. This plate bolts directly beneath the transparent dome and isolates the bubble area from the rest of the housing. The space between the plate and the bubble is temperature and humidity controlled with a heater-fan unit and a desiccant tray. This warm, dry environment prevents frost or dew

Figure 5. Photograph of the Instrument Showing the Dome and Scanning photometer and the Electronics Assembly.

accumulation. The Plexiglas bubble has a uniform transmission over all wavelengths of interest and transmits more than 91 percent of normally incident radiation. The other assembly within the unit is a 2-meter rack which supports most of the electronics that control the photometer, including the minicomputer (Interdata) and the dual magnetic cassette tape transport used for program loading and data recording.

III. CONTROL SYSTEM

The control system forms the heart of the instrument and is implemented via software on a 16-bit minicomputer. An overview of the software organization, followed by a more detailed discussion of individual modules, is presented below. The hardware requirements are simple and consist of the CPU, either 32 or 16 kilobytes of core memory, two magnetic cassette tape drives, and an interface board containing the circuitry necessary to control the instrument. Power switching to actuate the motors, brake, and clutch is accomplished with solid-state relays driven by logic-level signals. Similarly, input signals reporting the status of the instrument are derived from optoelectronic sensors when possible. This reduction of moving parts has led to a high degree of reliability in the instrument.

In many ways, the software is quite similar in organization to operating systems (OS) supporting multi-tasking typically found on larger machines. The role of the OS is distributed among several software modules. The foremost of these is the scheduler (SCHED) which acts as a task manager. In the present configuration, two tasks are resident—an observing control task (OBS) and a sun position calculation task (SUN). The primary function of SCHED is to decide which task is to run at any given time and to activate that task. This process occurs every 2 msec and is driven by an external clock interrupt. The OBS task is of higher priority than the SUN task and as such has first call upon the machine resources. It frequently enters a time interval wait state, however; and during this period, the sun position calculation is performed.

OBS is the central controlling task in the machine and calls upon one of two subroutines to carry out the desired function: GEPHY, the nighttime observing program, and SOLAR, for the daytime observing program. These are described in detail in Section IV. Support for these control functions is provided by a set of small routines partitioned into three levels.

Level 1 routines are driven by hardware interrupts and execute in a non-interruptable state—i.e., once started they proceed to completion without interference. They provide the following services: 1) writing the cassette tape; 2) maintaining the pointing direction of the instrument; and 3) providing operator-machine communication via the front panel control board.

Level 2 routines are those which require regularly scheduled operations and as such provide an operating background for the control task OBS. The functions include driving the front panel display, sampling the data values from the detectors, moving the instrument head, positioning the filter wheel and day-night slide, maintaining the date and time, and providing task interval waits.

Level 3 routines carry out task scheduling, task time waits, and setup of asynchronous I/O.

The sun position calculation task, SUN, requires only the date, time, and station latitude and longitude. Parameterized representations of the equation of time and the solar declination allow a calculation of the solar right ascension and declination. These values are then transformed to azimuth and elevation values via rotation algorithms. The calculation maintains an accuracy of ±0.5°.

The particular software philosophy used allows easy maintenance of the system since the structure is highly modular. In addition, since most of the machine control functions occur at a low level, changes in the operating program OBS are easily accomplished. The software has proven to be very stable. The only crashes which have

occurred over a 2-year period with nine machines are preprogrammed stops which halt the machine upon certain types of mechanical failure, beyond which continued operation would result in damage to the instrument. Updates and revisions of the software are accomplished by delivery to the field units of a cassette tape which is then loaded into each machine by the local operator.

Data acquired by the instrument are compressed before being written to magnetic tape. This affords a factor of two or more increase in running time between cassette-tape changes. Presently, a visit every four days is required to replace the cassettes. The data are recorded with an accuracy between 0.4 and 0.8 percent. Since it was desired to encode to a constant accuracy over a wide dynamic range and since successive samples of data often differ only slightly, the following encoding algorithm was used.

The algorithm successively left-shifts the 16-bit data value until the most significant bit is set. The shift count is added to the integration period used to acquire the value (see Section II) and a pseudo-period derived. The gain/pseudo-period byte is then compared with the previous value and is recorded only if a change occurred. The most significant byte of the data value is then recorded; this value lies between 128 and 255. To avoid oscillation at the decision point, an alternate scaling may be chosen. If the mantissa is scaled at 3/2 of its value, then the mid-range of the scaled mantissa will not intersect the mid-range of the unscaled mantissa. Thus when a gain/period byte change is required, the scaling which gives a mid-range value is chosen until another gain/period byte change is required.

IV. OBSERVATIONS

A. Aeronomy

The nighttime observing program is designed to obtain all-sky coverage of airglow emissions [OI] 557.7 nm and [OI] 630.0 nm, auroral emissions [OI] 557.7 nm, [OI] 630.0 nm, N_2^+ 427.8 nm, and

H_β 486.1 nm and the continuum at 535.0 nm. Five interference filters (Table 1) are used to select these wavelengths. The luminosity threshold varies from 2 Rayleighs (R) for units not located in the auroral zone to 10 R for units located in the auroral zone. The field of view is 2.5° for all units.

The observing technique consists of scanning the night sky in a series of almucantars at elevations 10°, 15°, 20°, 30°, and 50° for emission filters, and 10°, 26°, 42°, 58°, and 74° for the continuum filter. The geometrical circle of coverage depends on the altitude of the emission. For example, at 300 km, the 10° elevation scan has a radius of approximately 1150 km or 10° of geographic distance. For a 150-km emission altitude, the 10° elevation scan has a circle of coverage radius of approximately 650 km or 6° of geographic distance. Figure 6a illustrates the extent of the all-sky coverage obtained from the present eight locations of MASP units for 150-km altitude emissions and figure 6b for 300-km altitudes. The emission filter elevation scans were selected such that when constructing all-sky circle maps from the five elevation scans for an emission altitude of 300 km, the five concentric projection circles are approximately equidistant.

The number of samples taken at each elevation scan depends on the elevation of that scan and the auroral activity. With a field of view of 2.5°, an average integration period of 0.1 seconds, and a scanning rate of 20° per sec, the maximum sample rate used is one sample per 3° (120 samples per scan) in the 10° and 15° elevation scans. Allowing for the cosine effect of the sky solid angle covered for the other elevation scans, the maximum sample rates used are 90 samples per scan for elevation scans at 20° and 30°, and 60 samples per scan for the elevation scan at 50°. If the control program determines from the previous 630.0-nm all-sky scan that the auroral activity is low, the sample rates for the line emission filters all decrease by a factor of two. The sample rates for the

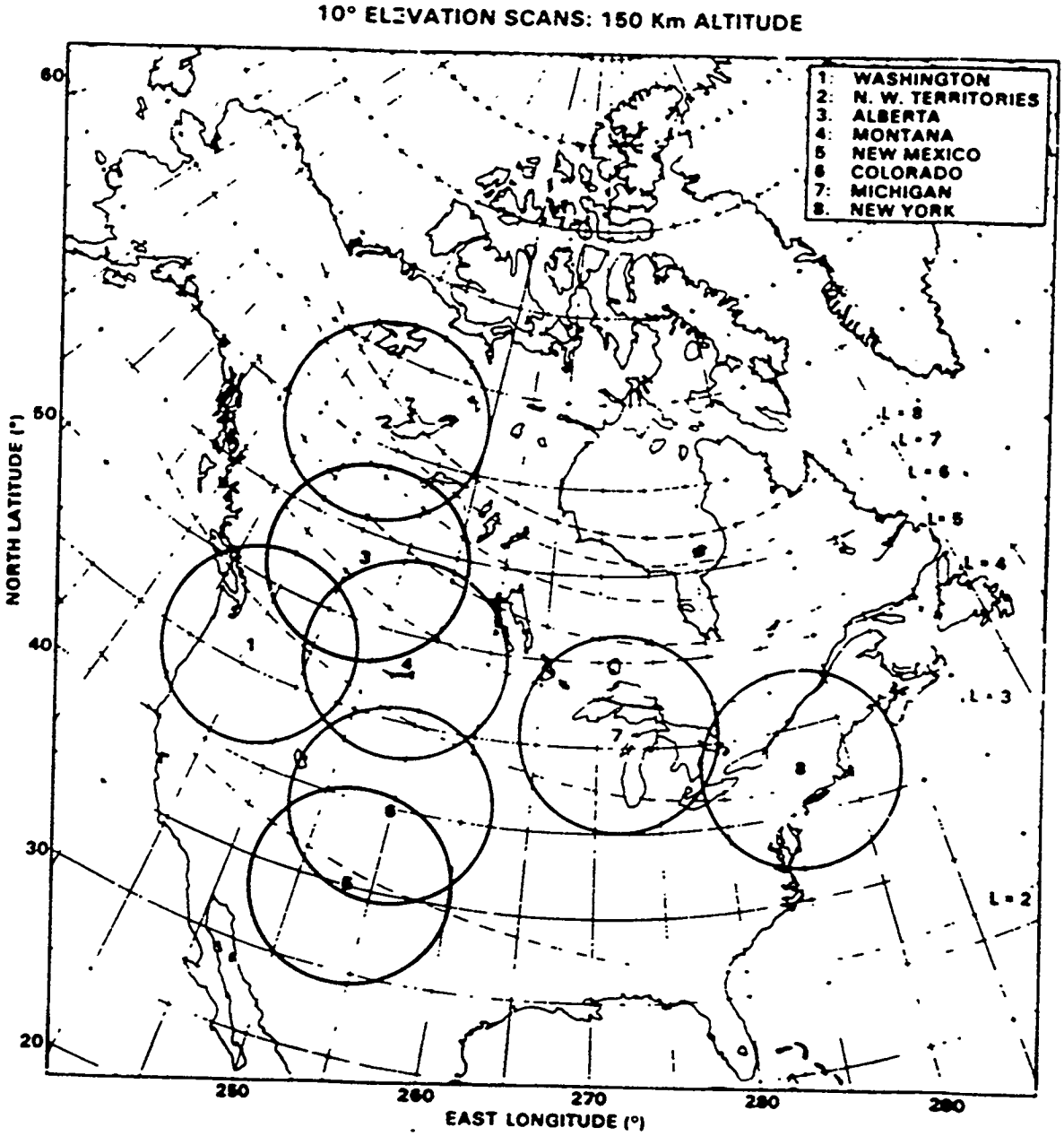

Figure 6a. The Field of Coverage for an Assumed Emission Height of 150 km.

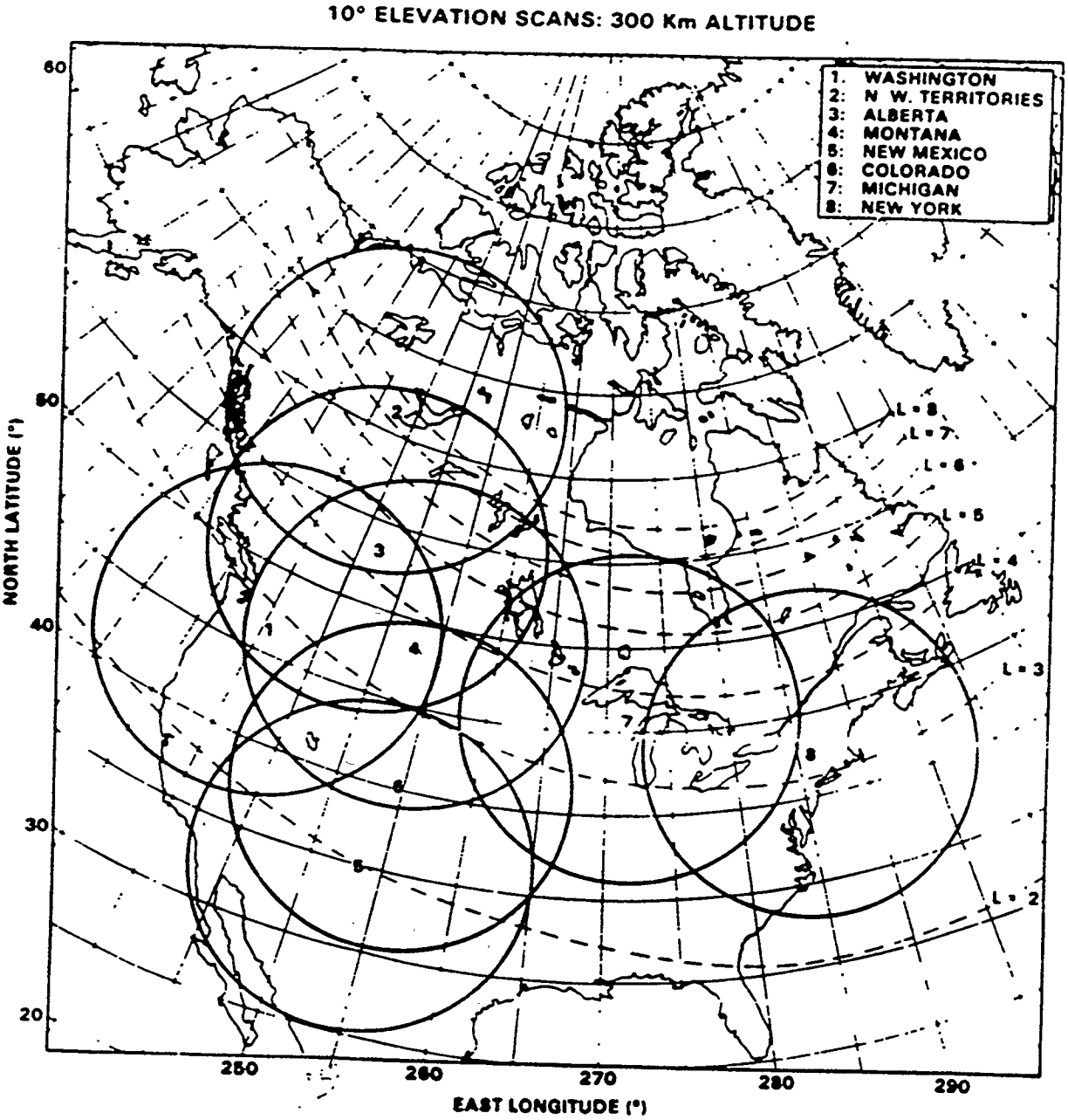

Figure 6b. The Field of Coverage for an Assumed Emission Height of 300 km.

continuum filter are always 120, 90, 72, 45, and 24 samples per scan for azimuth scans at elevations of 10°, 26°, 42°, 58°, and 74°, respectively.

One all-sky survey, which includes five almucantar scans plus zenith and dark-current measurements, takes 124 seconds. One set of 5-filter surveys takes 620 seconds. If it is determined from the previous 630.0-nm all-sky survey that the auroral activity is low, a set of 5-filter surveys is started on the hour and at every 20-minute increment from the hour. If the auroral activity is determined to be high, a set of 5-filter surveys is started on the hour and at every 12-minute increment from the hour. Sample data, unit identification, status information, date, and times are stored in memory until the storage reaches a pre-set number of bytes and then the buffer is written on the magnetic cassette tape and reset. Each cassette record, for active auroral periods, includes approximately two all-sky surveys.

The nighttime program runs whenever the solar elevation is depressed greater than 15° below the horizon and the date is not within two days of full moon. During full-moon periods no nighttime data are acquired.

B. Insolation

In the daytime measurements program, an attempt was made to design the operating routine to accommodate as many potential users of the data collected as possible. The direct solar data should be useful to central receiver power production facilities, to photovoltaic and photobiological conversion programs, and to radiative transfer theorists and climate modelers interested in the attenuation of solar radiation by atmospheric aerosols and water vapor. The diffuse radiation measurements should be especially helpful to those interested in the radiation transport properties of clouds, to aerosol physicists and chemists, and to low-temperature solar

collector designers and architects. The next few paragraphs outline the basic routine employed at all photometer sites.

Figure 7 illustrates the sequence of measurements that begins at sunrise and is repeated every 30 minutes until sunset. Every 5-minute time slice begins with a direct measurement of the sun. The straightforward procedure of pointing directly at the sun cannot be confidently employed. The sun's position is calculated once per minute to an accuracy of ±0.5°. The pointing accuracy of the instrument is ±0.3°. The largest error in pointing by dead reckoning, however, ordinarily occurs in the alignment of the instrument. In principle, it may be aligned to within 0.5° but only after a great deal of painstaking effort. In view of these considerations, one cannot be certain that the sun is entirely within the 1.5° field-of-view aperture at all times. To make the direct measurement then, a sun-centered raster scan is made. This scan has dimensions 5° in azimuth by 3° in elevation with samples taken every 0.5° in azimuth and every 0.3° in elevation, generating 110 samples of which only the largest is retained along with its location in the scan. The scan is repeated for each of the seven solar filters during the first part of each 5-minute time slice, except during the first and fourth time slices of the 30-minute sequence when there is sufficient time to sample all 12 filters. During the second 5-minute time slice of the 30-minute sequence, a solar almucantar scan is performed in each of the solar filters. A solar almucantar scan is a revolution in azimuth at the solar elevation. The first sample is taken 5° in azimuth from the sun with subsequent sampling every 5° to 180° from the sun. The third and fourth time slices sample in a similar manner except the scanning is in elevation starting 5° above the sun and continuing to the opposite horizon. Two scans are required because the elevation scan rate is one-fourth that of the azimuth. The fifth and sixth scans sample the diffuse sky roughly every 10°. The scans are almucantars at every 10° of elevation. The azimuth spacing of the samples is scaled as the sine

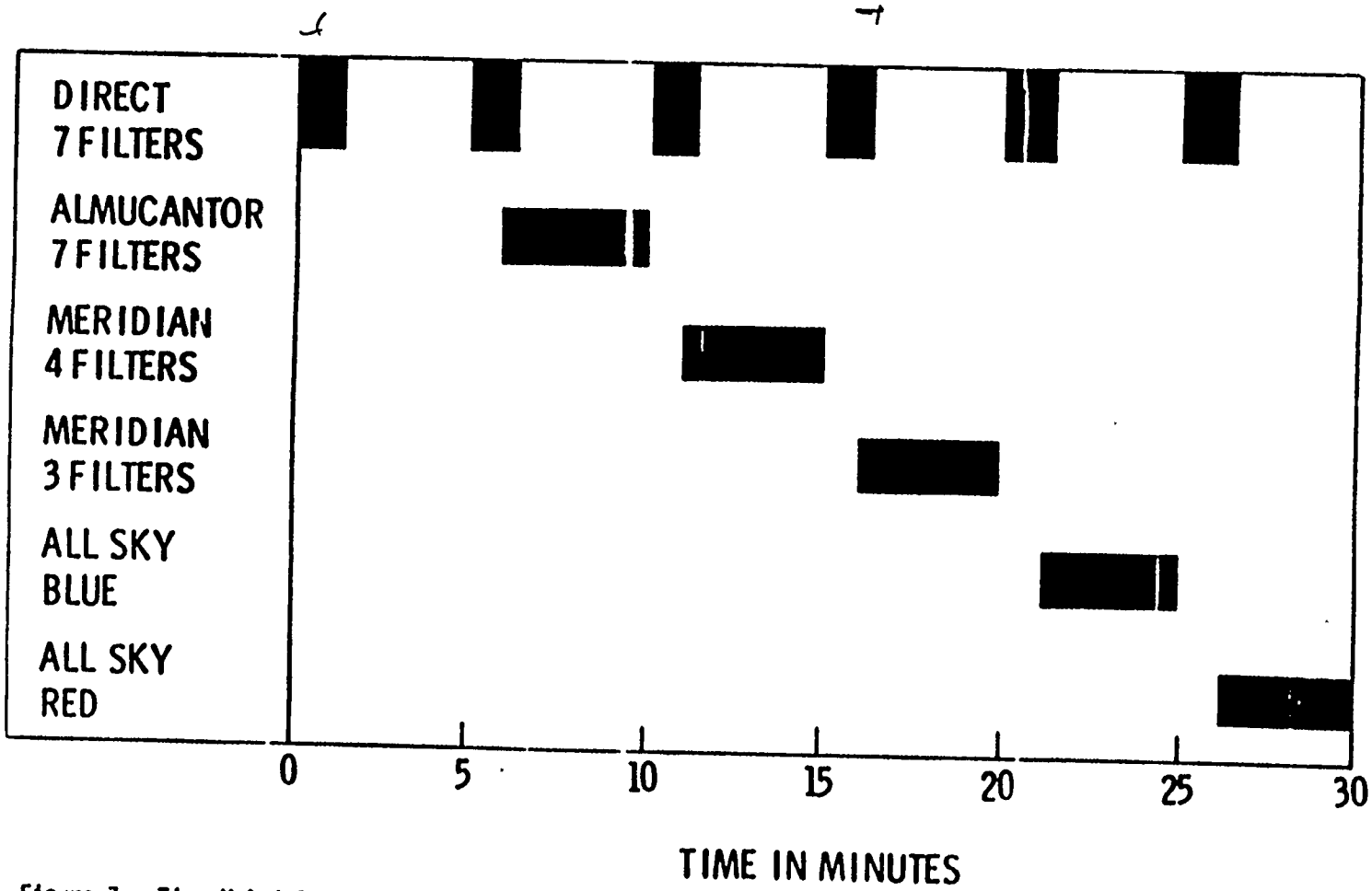

Figure 7. Time Multiplex Frame for Solar Measurements.

of the elevation angle. A broad red filter scan in the sixth time slice follows a broad blue filter scan in the fifth time slice.

The control program writes a variable length record in an attempt to efficiently record the data, i.e., minimize the ratio of inter-record gap to total record length. It provides for power-fail recovery, and it writes an identifiable record at day's end. At night, it takes samples, after the F1-M3 assembly of figure 1 is removed, to determine the number of counts due to the offset voltage on the photodiode, i.e., dark count.

C. Other Programs

The idea of allowing most of the decision-making to be incorporated within the software allows new observational requirements and requests to be handled rather easily. One program, which has proved very useful, is a utility program used to check the operation of the unit, to calibrate the unit, and to run special experiments using the routine scan patterns of the instrument.

Two recent examples illustrate the ease with which new experiments may be implemented. A request was received to study the diffusion properties of a "charge" of ionized material released from a rocket in the ionosphere. The program to accomplish this was a hybrid version of software that already existed for the routine nighttime monitoring and the utility program described above and, consequently, required only a few days to code and debug. Another request involved the measurement of diffuse data sampled over the hemisphere in five broad filters as input to an architectural model employing sunlight for interior lighting. This required less than an afternoon to implement. Not all future requirements will be this straightforward, but most will be able to build on the extensive software that already exists.

V. CALIBRATION

All of the current programs using the mobile automatic scanning photometer require that the photometer make absolute measurements.

Outlines of the methods employed in calibrating the two detectors are given below.

A. Aeronomy

A wide-aperture standard light obtains its primary calibration via a transfer comparison against a Carbon 14 activated phosphor light source as described by Smith and Alexander (1963). It has also been intercompared with the University of Michigan's and the University of Alaska's calibrated lamp sources in order to establish a coordinated network of standard sources. The MASP unit is calibrated by positioning the standard lamp directly in front of the scanning head such that the source fills the field of view. A calibration program, run on the MASP central processor, records alternately the photometer tube output and the output of the lamp sensor (described later) for the solar and aeronomy filters. The accuracy of the absolute calibration is approximately 20 percent.

Figure 8 illustrates the important features of the wide-aperture standard lamp which consists of two diffusing cavities. The first small cavity houses a GE 3026 halogen cycle miniature lamp, L1, which is driven by a constant-current power supply. The lamp is positioned within the cavity such that the first baffle, B1, shields the aperture, A1, from direct illumination. Thus the light must be scattered at least once from the flat white interior of the cavity before exiting the aperture. A Schott #FG-4 filter, F1, is placed just ahead of the aperture in order to increase the apparent color temperature of the light source.

The second cavity is a standard aluminum instrument case measuring 45 cm x 60 cm x 50 cm deep, the interior of which has been painted flat white. A second baffle, B2, is placed so as to shield the first diffusor, DF1, from direct illumination from the aperture. A second smaller diffusor, DF2, is placed after the first one which serves as the exit pupil of the instrument. The diffusing disks are 0.3-cm thick, milk-white Plexiglas which has proven to be comparable to opal glass in its diffusing properties.

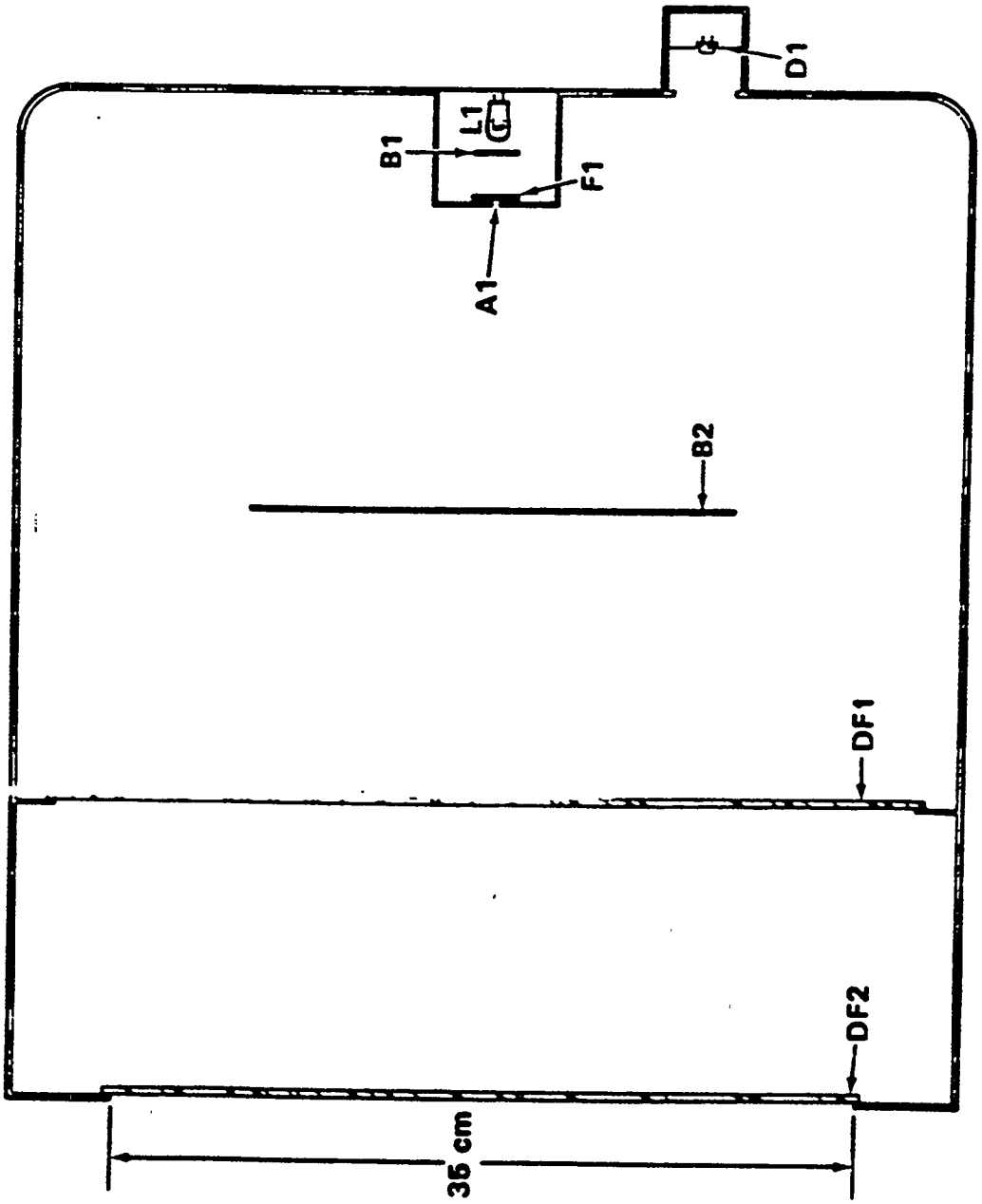

Figure 8. Wide-Aperture Calibration Light Source.

The lid of the case houses the two power supplies—one for the lamp previously described and a smaller power supply for the optical sensor, D1, whose function is to monitor the light output reflected from the second baffle. The lamp power supply is a constant-current design and in practice maintains the lamp output constant to better than 1 percent. The optical sensor consists of a silicon PIN photodiode (RCA 30808) and a high-gain LM308AN op amp, the output of which is supplied to the multiplexer input of the MASP central processing unit for data recording.

B. Insolation

In order to achieve an absolute calibration of the solar photometer, an active cavity radiometer (ACR) is used (Radiometrics Corporation). The ACR has proven a reliable instrument for the absolute measurement of solar radiation. This type of instrument was responsible for defining the 2.2-percent error in the International Pyheliometric Scale. This absolute pyrheliometer is described by Willson (1973) and is essentially a light-absorbing cavity wound with a resistance heater and a resistance thermometer. Absolute power measurements are made by heating the cavity to a given temperature with and without radiation incident on the cavity. The difference in power requirements is the absolute value of the incident radiation, aside from a calibration constant near 1.

The mobile photometer is calibrated on clear, cirrus-free days as close to solar noon as possible. Each sun-looking reading of the ACR is sandwiched between two dark readings of the ACR. Since the ACR has a 2-second time constant, approximately 30 seconds is allowed to elapse before 12 consecutive readings, one-half second apart, are made. By averaging the 12 readings, we arrive at a more accurate value of the power levels. Each ACR measurement is immediately followed by a photometer measurement of the solar flux through the same filter. There is an approximate delay of 45 seconds between measurements on the two instruments. By measuring

near noon when the solar elevation changes little and by making measurements with as little delay as possible, a calibration accuracy of 1 percent or better is obtained on the high-throughput filters. The measurement for any particular filter is repeated several times and then averaged to arrive at a calibration factor for each filter.

There was some concern that the changing incident spectral distribution of the sun as the airmass increased would necessitate an airmass-dependent calibration. The effect would be strongest in the blue-ultraviolet region of the spectrum where the strong λ^{-4} Rayleigh scattering extinction coefficient is most pronounced. An airmass-dependency study in the broad blue filter was made to check this effect. No statistically significant change over five airmasses was detected.

VI. NETWORK DESCRIPTION

Three funding agencies have contributed to the development of the photometers, each with different requirements for their program. Three of the units were funded to provide aeronomical observations during the International Magnetospheric Study; two of the units were funded to take site-specific solar data; and the five remaining units were to provide both daytime and nighttime measurements. These considerations account for the geographical distribution of mobile automatic scanning photometers given in figure 6.

There were north-south and east-west chains of photometers. The north-south chain included Fort Providence (Northwest Territories, Canada), Leduc (Alberta, Canada), Hinsdale (Montana), Boulder (Colorado), and Albuquerque (New Mexico). The east-west chain included Richland (Washington), Hinsdale (Montana), Iron Mountain (Michigan), and Albany (New York). There were eight stations rather than ten because two units were retained for special-purpose use, e.g., nonroutine experiments or non-network filters. This geographic arrangement existed for more than two years and is now being revamped due to programmatic changes.

ACKNOWLEDGEMENTS

The authors are especially indebted to Karl Davis who provided important software contributions to the project. Philip Ekstrom was responsible for the original controller design for the cassette tape drives before a change to the present commercially available units was required. Financial support of the long-term development of the units was provided by the Office of Basic Energy Sciences within the Department of Energy. Additional support was provided by the Office of Conservation and Solar Energy within the Department of Energy and by the National Science Foundation's Atmospheric Sciences Program (ATM78-12313 01).

REFERENCES

"Silicon Photovoltaic Detectors and Detector/Amplifier Combinations." July 1981. Application Notes D3011C-5, EG&G Electro-Optics, Salem, MA, USA.

Smith, L. L. and R. B. Alexander. 1973. "Airglow." International Solar Quiet Year Manual No. 5, p. 25, London.

Willson, R. C. 1973. "Active Cavity Radiometer." Appl. Opt. 12:810-817.

Kleckner, E. W., L. L. Smith and R. J. Hoch. 1975. "A Multipurpose Instrument for Solar Radiation Measurements." In Proceedings of the SPIE 19th Annual Technical Symposium: Optics in Solar Energy Utilization, 58, ed. Yale H. Katz, pp. 68-74. Published by the SPIE, 338 Tejan Place, Palos Verdes Estates, CA 90274.

Kleckner, E. W., J. J. Michalsky and L. L. Smith. 1978. "Multispectral Measurement of Direct and Diffuse Solar Radiation at Ground Level." In Proceedings of the American Section of the International Solar Energy Society, eds. Karl W. Böer and Gregory E. Franta, Vol. 2.2, pp. 676-680. Published by Publishing Office of the American Section of the International Solar Energy Society, Inc., McDowell Hall, University of Delaware, Newark, DE 19711.

INTERNAL DISTRIBUTION

1. D. Alvic, UT/EERC
2. J. Barkenbus, UT/EERC
3. L. D. Bates, K-1201, MS-7256
4. T. W. Beaty, 1507, MS-6407
5. B. A. Bervin, 4500S, MS-6124
6. T. A. Boden, 1000, MS-6335
7. M. D. Burtis, 1000, MS-6335
8. J. B. Cannon, 4500N, MS-6189
9. R. B. Cook, 1505, MS-6038
10. J. H. Cushman, 1503, MS-6352
11. R. M. Cushman, 1000, MS-6335
12. V. H. Dale, 1505, MS-6035
13. R. C. Daniels, 1000, MS-6335
14. N. T. Edwards, 1506, MS-6034
15. M. P. Farrell, 4500N, MS-6250
16. D. E. Fowler, 1505, MS-6035
17. S. G. Hildebrand, 1505, MS-6037
18. G. K. Jacobs, 1505, MS-6036
19. S. B. Jones, 1000, MS-6335
20. D. P. Kaiser, 1000, MS-6335
21. P. Kanciruk, 1507, MS-6407
22. A. Kozyr, 1000, MS-6335
23. J. M. Loar, 1504, MS-6351
24. G. Marland, 1000, MS-6335
25. L. J. Morris, 1000, MS-6335
26. T. R. Nelson, 1000, MS-6335
27. D. E. Reichle, 4500N, MS-6253
28. R. J. Sepanski, 1505, MS-6035
29. F. E. Sharples, 1505, MS-6036
30. D. E. Shepherd, 1507, MS-6407
31. D. S. Shriner, 1505, MS-6038
32. J. W. Simmons, 2506, MS-6039
33. T. Stamm, UT/EERC
34. S. H. Stow, 1505, MS-6038
35. P. L. Sullenberger, 1000, MS-6335
36. Central Library, 4500N, MS-6291

37-51. ESD Library, 1505, MS-6035

52-53. Laboratory Records, 4500N, MS-6285

54. Laboratory Records Dept., ORNL-RC
55. ORNL Patent Section, 4500N, MS-6258
56. ORNL Public Relations, 4500N, MS-6213
57. ORNL Y-12 Tech. Library, 9711-1, MS-8104

EXTERNAL DISTRIBUTION

58. J. Barnard, Pacific Northwest Laboratory, P.O. Box 999, Richland, WA 99352-0999
59. B. A. Bodhaine, NOAA/CMDL, R/E/CG-1, 325 Broadway, Boulder, CO 80303
60. M. Broido, Acting Director, Environmental Sciences Division, U.S. Department of Energy, 19901 Germantown Road, Germantown, MD 20874
61. A. Clark, Department of Oceanography, University of Hawaii, 1000 Pope Road, Honolulu, HI 96822
62. F. A. Donath, Director, Institute for Environmental Education, Geological Society of American, 1006 Las Posas, San Clemente, CA 92673
63. C. E. Duchon, School of Meteorology, 1310 Sarkeys Energy Center, Univ. of Oklahoma, Norman, OK 73019
64. E. Dutton, NOAA/CMDL, R/E/CG-1, 325 Broadway, Boulder, CO 80303
65. R. N. Farvolden, Professor, Department of Earth Sciences, University of Waterloo, Waterloo, Ontario N2l 3G1
66. B. Forgan, Bureau of Meteorology, 150 Lonsdale Street, Melbourne, Victoria 3001, AUSTRALIA
67. D. W. Freckman, Director, College of Natural Resources, 101 Natural Resources Building, Colorado State University, Fort Collins, CO 80523
68. Lee Harrison, Atmospheric Sciences Research Center, 100 Fuller Road, Albany, NY 12205
69. R. B. Husar, Washington University, Center for Air Pollution Impact and Trend Analysis, St Louis, MO 63130-4899
70. H. Jaeger, Fraunhofer Institut fuer Atmosphaerische Umweltforschung, Kreuzeckbahnstr. 19, D-82467 Garmisch-Partenkirchen, GERMANY

71-80. N. R. Larson, Pacific Northwest Laboratory, P.O. Box 999, Richland, WA 99352-0999

81. N. Laulainen, Pacific Northwest Laboratory, P.O. Box 999, Richland, WA 99352-0999
82. J. Livingston, SRI International, 333 Ravenswood Ave., Menlo Park, CA 94025

83. B. A. LeBaron, Utah Bureau of Air Quality, 1950 West North Temple, P.O. Box 16690, Salt Lake, UT 84116-0690
84. J. J. Michalsky, Atmospheric Sciences Research Center, 100 Fuller Road, Albany, NY 12205
85. D. Nelson, NOAA/CMDL, R/E/CG-1, 325 Broadway, Boulder, CO 80303
86. P. Novotny, Bureau of Meteorology, 150 Lonsdale Street, Melbourne, Victoria 3001, AUSTRALIA
87. J. A. Ogren, NOAA/CMDL, R/E/CG-1, 325 Broadway, Boulder, CO 80303
88. S. Oltmans, NOAA/CMDL, R/E/CG-1, 325 Broadway, Boulder, CO 80303
89. Bobbi Parra, Environmental Sciences Division, Office of Health and Environmental Research, ER-74, U.S. Department of Energy, Washington, DC 20585
90. A. Patrinos, Associate Director, Office of Health and Environmental Research, U.S. Department of Energy, G-165, Germantown, MD 20874
91. G. S. Sayler, Professor, 10515 Research Drive, Suit 100, The University of Tennessee, Knoxville, TN 37932-2567
92. B. A. Schichtel, Washington University, Center for Air Pollution Impact and Trend Analysis, St Louis, MO 63130-4899
93. D. Slater, Pacific Northwest Laboratory, P.O. Box 999, Richland, WA 99352-0999
94. G. Stokes, Pacific Northwest Laboratory, P.O. Box 999, Richland, WA 99352-0999
95. L. Thomason, Atmospheric Sciences Division, MS-475, NASA Langley Research Center, Hampton, VA 23681
96. O. Torres, Hughes STX, Commerce Center 1, 7701 Greenbelt Road, Suite 400, Greenbelt, MD 20770
97. M. Wesely, Building 203, ER, Argonne National Laboratory, Argonne, IL 60439
98. F. J. Wobber, Environmental Sciences Division, Office of Health and Environmental Research, ER-74, U.S. Department of Energy, Washington, DC 20585
99. Office of Assistant Manager for Energy Research and Development, U.S. Department of Energy, Oak Ridge Operations, P.O. Box 2001, Oak Ridge, TN 37831-8600

100-101. Office of Scientific and Technical Information, P.O. Box 62, Oak Ridge, TN 37831